Biophysical Characterization of Cancer Cell Phenotypes

by

Nethmi Ariyasinghe

A Dissertation Presented in Partial Fulfillment
of the Requirements for the Degree
Doctor of Philosophy

Approved April 2019 by the
Graduate Supervisory Committee:

Robert Ros, Chair
Stuart Lindsay
Peiming Zhang
Sara Vaiana

ARIZONA STATE UNIVERSITY

May 2019

ABSTRACT

Cancer is a serious health concern. Current treatments are limited due to certain subpopulations of cancer cells being resistant to chemotherapy and radiation. These subpopulations have been qualitatively identified but much work remains to quantify the abnormalities they exhibit such as irregular nuclear shape. This dissertation seeks to determine physical science methods which can identify and quantify the biological characteristics of cancer and non-cancer cells. For the first project, the deoxyribonucleic acid (DNA) and chromatin of cancer and non-cancer esophageal cells were quantified using spectrophotometry and atomic force microscopy. Then the cellular nucleus shape, chromocenters, nucleoli, and nuclear speckles were characterized using 3-D confocal microscopy. A majority of a cell's DNA is isolated in the supernatant fraction during salt fractionation for both cancer and non-cancer. Additionally, the nuclear size of cancer cells is roughly twice that of non-cancer cells due to the increased ploidy of the cancer cell line (more chromatin) and this chromatin exists in a less decondensed state than that of the chromatin in non-cancer cells. Then using combined atomic force microscopy and CLSM, the Young's modulus of cancer stem-like cells and non-stem-like cells were characterized for three breast cell lines: MDA-MB-231, MCF-7, and MCF-10A. It was determined that the MCF-7 is impacted by buffer environment whereas the MDA-MB-231 and the MCF-10A cell lines are not. MCF-7 cells are stiffer when measured in Phosphate Buffer Solution (PBS) compared to Hank's Balanced Salt Solution (HBSS) buffer possibly due to the fact that HBSS buffer tends to enhance the Warburg effect on cell lines. Additionally, there is a significant stiffness difference between stem cells and non-stem cells in the MCF-7 cell line which does not occur in the MDA-MB-231 cell line for the larger tip. These differences could be attributed to differences in cell phenotype for the cell lines. MDA-MB-231 cells are mesenchymal so it agrees with the hypothesis that there is no difference between cancer stem cells (CSCs) and non-CSCs cell stiffness; on the other

hand the MCF-7 cell line is luminal so the CSCs being more mesenchymal-like would be softer than the non-CSCs.

DEDICATION

To my parents and sister for their unconditional support

ACKNOWLEDGEMENTS

This dissertation would not be possible with the support of my colleagues, fellow students, and faculty at Arizona State University and other institutions. First I would like to thank my graduate advisor for his help and support during the undertaking of this dissertation as well as my other committee members for their guidance. Additionally, I would like to thank the members of the Ros lab group both past and present: Olaf Schulz for his guidance and help with atomic force microscopy and confocal microscopy, Rory Staunton for his assistance with understanding the mechanics of cancer biology, Bryant Doss for his guidance throughout my time in the lab, Nikita Satapathy for support with cell culture, Brendan Sullivan for teaching me the chromatin and DNA extraction protocols, Ben Miller for his support in purifying reagent for chromatin experiments, Miles Piper for his assistance in chromatin imaging, James Faust for his assistance with 3-D confocal imaging of cellular nuclei, and Rodrigo Gutierrez for his assistance with cell culture. Finally, I would like to thank Kerinna Coffey for her assistance in proofreading this dissertation.

Contents

List of Tables

List of Figures

Chapter 1

Introduction

One in every four deaths in the United States is related to cancer [1]. In 2018, it is estimated that there will be 1,735,350 new cancer cases as well as 609,640 deaths from cancer [1]. While much has been done to create innovate therapies to target as well as treat the disease, there is still a lot of information that is unknown about cancer. Biology has done much to characterize and identify traits of the disease on a qualitative level, but has not been able to quantify these traits. For example, it is know that a visually abnormal cellular nucleus is a sign of cancer or an indication of worsening prognosis [2, 3, 4, 5]; however, not much has been done in the way of trying to quantify nuclear abnormality. This is where the knowledge gap can be bridged by using the physical sciences to quantify qualitative biological characteristics. The goal of this dissertation is to utilize quantitative, physics-based approaches to understanding the current qualitative characterizations of cancer biology.

Chapter 2 introduces key concepts that are known in regards to cellular biology, chromatin, DNA and cell markers which serve as a background for certain measurements taken during experimentation and as a motivation for this thesis. Chapter 3 discusses the experimental techniques utilized for this dissertation.

Chapter 4 discusses the quantification of DNA for two esophageal cell lines as

well as the contents of the S_0 (the fraction extracted from the supernatant created right after the Mnase digestion of the chromatin) after the use of the salt fractionation technique developed by Marilyn Sanders in 1978 failed to account for 30% of extracted DNA. The goal of this project sought to (1) determine the reason for DNA unaccounted for in salt fractionation experiments, (2) quantify the relative amount of DNA in each cell line, and (3) characterize the differences in the nuclei of cancerous and non-cancerous cell lines.

Chapter 5 seeks to determine if there is a correlation between breast CSCs and stiffness by combining confocal with AFM to directly correlate CD44/CD24 fluorescence levels with stiffness at the single cell level. It is hypothesized that since CSCs have been shown to correlate with the mesenchymal phenotype and follow some of the same pathways as the epithelial-to-mesenchymal transition that the CSCs would be softer than non-CSCs. Additionally, this experiment seeks to determine (1) if different buffer/environment conditions (PBS vs. HBSS) affect the stiffness of the different subpopulations (2) if it is possible to distinguish differences between the cellular cortex and intracellular network of CSCs and non-CSCs and (3) if there is a difference in the Young's Modulus of CSC and non-CSC nuclei.

Chapter 2

Biological Concepts and Cell Mechanics

2.1 DNA, Chromatin, and Chromatin Organization in a Cell

Watson and Crick described the structure of Deoxyribonucleic Acid (DNA) in 1953: a molecule with complementary base sequences on two strands and a right-handed double helical nature with adenine (A) complementary to thymine (T) and guanine (G) complementary to cytosine (C) [6]. DNA contains the hereditary information for all living organisms. To fit the entire genome into a tiny cell, the DNA is coiled and compacted around histones which then form nucleosomes and chromatin as shown in **Figure 2.1**. In general, the coding regions of the DNA have a G/C rich region whereas the non-coding regions of DNA sequences are generally more A/T rich [7, 8]. This implies that structurally coding sequences are stiffer whereas non-coding sequences are more flexible and more prone to strand separation. In contradiction, eukaryotic chromosome coding sequences have a higher nucleosome occupancy than non-coding sequences serving as potential topological sinks to signal transcription

sites for enzymes [9].

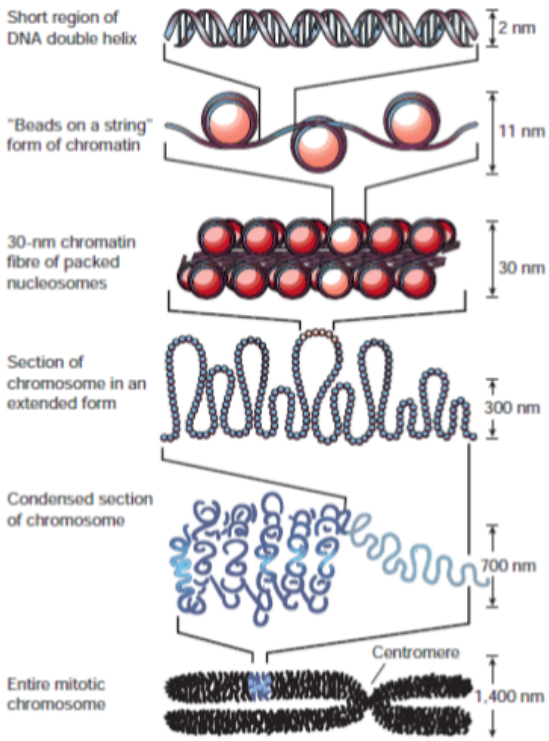

Figure 2.1: Chromatin Structure [10]

Chromatin is the substance through which eukaryotic cells package their genetic information. It is a mix of DNA and structural and regulatory proteins that is normally found as a 30 nm fiber in eukaryotes. The most basic unit of chromatin is the nucleosome [11] which consists of 160-200 DNA base pairs wrapped twice around an octomer of core histones (H2A,H2B,H3,H4) and is sealed with a linker histone (H1 and H5) [12, 13]. A histone is an octomeric protein that is made of eight subunits: two H2A and H2B dimers and a H3-H4 tetramer [12, 13]. The nucleosome enables a five to tenfold compaction of the DNA [14]. Core histones are positively charged proteins with large amounts of lysine and arginine that bind directly to the DNA fiber through noncovalent forces [15].

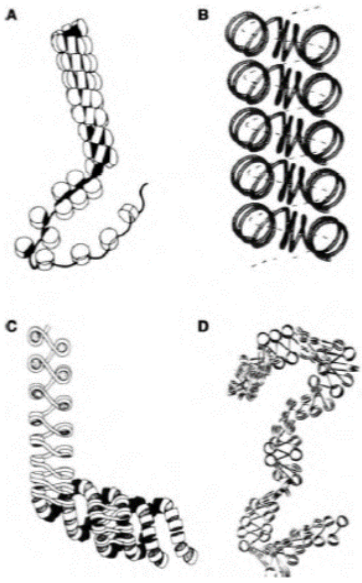

Figure 2.2: Four Models of the Higher Order Structure of Chromatin [15]

The higher order structure of the 30 nm chromatin fiber is controversial. The four models shown in **Figure 2.2** are the most current hypotheses. Current experimental data suggests that the most likely structure for the chromatin is the solenoid model (**Figure 2.2A**) [15].

There are two subcategories of chromatin: euchromatin and heterochromatin. Euchromatin has a more open or accessible structure for transcription with more loosely connected nucleosomes to the DNA giving it the appearance of a structure resembling beads on a string. Heterochromatin has a highly condensed structure that is hard to transcribe [16]. Heterochromatin replicates later in the S phase of the cell cycle and is found only in eukaryotes unlike euchromatin which is found in both eukaryotes and prokaryotes [17]. DAPI or a DNA dye stains heterochromatin brightly and can be used to differentiate between the two types of chromatin. In mammalian cells heterochromatin is composed of tandem repeats and remains condensed throughout the cell cycle. Additionally, compact chromatin generally represses DNA interactions and inhibits the movement of RNA polymerases [15].Constitutive heterochromatin is

defined by chromatin structures that remain compacted throughout interphase and is usually associated with C bands on mitotic chromosomes [18]. It is identified chemically by tri-methylation of H3K9 and monomethylation of H3K27. Facultative heterochromatin is defined by regions that condense after cell differentiation, having certain distinctive chemical features also, in case of, for example, Barr bodies. Gene expression is affected by location of the gene in relation to heterochromatin, [18] not surprisingly, given that heterochromatin is more compact than euchromatin. However, many genes in heterochromatin are actively expressed and many genes in euchromatin are inactivated [15]. Evidence that heterochromatin really is compacted (as opposed to just looking that way in stained cells) comes from sedimentation studies of satellite-containing regions [19]. A more recent genome-wide study in which open and compact chromatin was separated using sucrose sedimentation [15] shows that compact chromatin can be found in both heterochromatin and euchromatin regions (as defined by chromatin that hybridizes with labeled DNA taken from the C and G bands of mitotic chromatin). And while more genes are located in open chromatin, there is little difference in gene expression between the two fractions. In light of this, Gilbert et al. [15] suggest that the major role for chromatin compaction lies in organizing chromatin so as to cluster related genes together. In the absence of whole genome sequencing studies, the possibility remains that a small fraction of genes, critical to the phenotype, are affected by chromatin compaction. Electron microscopy shows that chromatin reconstituted in low salt has an open beads-on-a-string structure, turning into more condensed 30 nm fibers at higher salt [20]. These fibers have been observed in chromatin extracted from cells [21] and in reconstituted chromatin imaged by cryomicroscopy [22], though their existence in-situ is disputed [23]. A large majority of chromatin extracted from cells exhibits a much more complex structure composed of 60 to 130 nm chromonema fibers [24, 25]. None of these studies have attempted to sort the chromatin into open and compact fractions prior

to imaging, so the correlation between these reported structures and the open and compact fractions revealed by sedimentation is not established [15, 19].

Modifications of chromosomal components have a regulatory function in chromosomal segregation, replication, and repair and are correlated with specific histone modifications [15]. These types of modifications are known as epigenetics since they are heritable changes in gene expression that are not accompanied by DNA sequence changes [15]. For example, histone acetylation makes chromatin accessible to DNA binding proteins by destabilizing the nucleosomes and causes transcribing to proceed more efficiently [15]. The six hallmarks of cancer described by Hanahan and Weinberg in 2000 (resisting apoptosis, self-sufficiency in growth signals, insensitivity to anti-growth signals, invasive metastasis, unlimited cellular proliferation, and sustained angiogenesis) can be seen on a fundamental level as a deregulation of gene expression at the transcriptional level [15]. For example, a misuse of histone deacetylase leads to an uncontrolled proliferation of myelocytes causing acute myloid leukemia in humans [15]. Additionally, recent genome sequencing studies have uncovered cancer-associated mutations in genes that encode chromatin regulatory factions and enzymes; a few of these discoveries are discussed below [15].

Enhancers are non-coding DNA portions that serve an essential role in transcriptional regulation by creating tissue-specific gene expression patterns [15]. The precise manner in which enhancers act is not fully understood; however, they can act across long ranges of DNA to activate a specific promoter [15]. These enhancer-promoter communications involve the formation of chromatin loops mediated by cohesin complexes [15]. Recent genome-wide studies have identified mutations in genes that regulate enhancer chromatin in cancer which raises the possibility that mutations in these regions may lead to compromised enhancer-promoter communication allowing for activation of oncogenic genes [15]. Additionally, studies of chondroblastoma and giant cell tumors of bone have shown histone H3.3 gene mutations associated with dis-

tinct disease phenotypes [26]. 95% of chondroblastoma samples anlyzed in the study had a mutation of the H3.3 gene at Lys36 to methionine (H3.3K36M) in the H3F3B gene; 92% of giant cell tumors of bone had mutations of H3.3Gly34 to tryptophan or leucine [26]. Finally, work in follicular lymphoma has identified mutations in the histone H1 genes [15]. Since histone H1 acts as a linker histone and is responsible for chromatin compaction, this suggests that mutations in histone H1 may lead to errors in chromatin compaction and cause transcriptional misregulation.

Given then that open and compact chromatin do not correspond simply to euchromatin and heterochromatin, this dissertation seeks to determine if there are distinctive structural differences between the chromatin of cancer and non-cancer cells and how epigenetic modifications impact the progression of cancer.

2.2 The Basic Structure of a Mammalian Cell

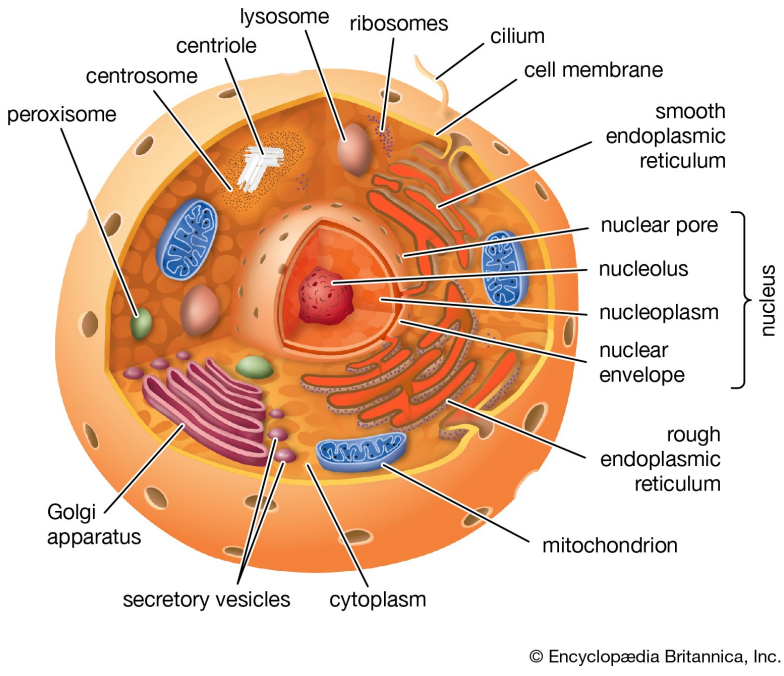

Figure 2.3: The Structure of a Mammalian Cell [27].

Figure 2.2 shows the structure of a mammalian cell. The most important feature of a mammalian cell is the compartmentalization of the organelles which carry out specialized functions [28]. The largest organelle is the nucleus which is roughly spherical in shape and stores all of the cells genetic information. Additionally, many nuclei have a darker staining region called the nucleolus were the synthesis of ribosomal RNA takes place [28].

The cytoplasm of all eukaryotic cells contains a network of protein fibers that support the shape of the cell called the cytoskeleton [28]. The cytoskeleton is a dynamic system that constantly forms and disassembles with individual fibers forming via polymerization. There are three types of cytoskeletal fibers: actin filaments, microtubules, and intermediate filaments [28]. Actin filaments are about seven nanometers in diameter and is composed of two protein chains loosely intertwined. Cells regulate the rate of actin filament formation and these filaments are responsible for cellular movements such as contraction [28]. Microtubules are hollow tubes about twenty five nanometers in diameter. They allow for cellular movement and help move materials within the cell as well [28]. The strongest part of the cytoskeleton are the intermediate filaments, named because they are 8-10 nanometers in diameter and are intermediate in size between actin filaments and microtubules. The most common type of intermediate filaments are vimentin [28].

2.3 Definition and Characteristics of Stem Cells

A stem cell is defined as a cell that is able to produce progeny that are able to differentiate into multiple types of specialized cells (heart cell, lung cell, etc) as well as the ability to self-renew in the undifferentiated state [29]. Initially, every human begins as a single egg fertilized by a sperm. As the single cell divides to form a multicellular organism, it is stem cells that are created and begin to form the heart,

lungs, and other organs of the organism. However, at some point during the creation of the organism, the majority of the cells lose their ability differentiate into other types of cells and thus, cease to be stem cells [29]. However, the ones that do retain their stem cell capabilities have a very important role in the adult organism: to repair and create additional cells for damaged tissues in the body [29]. In an adult organism, the role of the stem cell is to create progeny identical to the parent cell (self-renewal), to create progeny that are differentiated into a particular tissue lineage, and to regulate the acts of self-renewal and differentiation (homeostasis) [29]. It is also important to note that stem cells in different areas of the body regenerate at different rates. Stem cells in the bone marrow regenerate at rapid rates whereas stem cells in the colon regenerate more slowly [29]. Also stem cells in areas of the brain are only activated if tissue damage occurs [29].

2.4 Cancer Stem Cells

Building upon this then, characteristics of cancer stem cells include the ability to self renew and differentiate, the ability to persist in the body for long periods of time, and the ability to produce heterogeneous progeny [30]. The CSC concept treats tumor cells as a diverse population where only certain cells (the CSC cells) have the ability to proliferate extensively and potentially form new tumors. In contrast, the older tumor model assumed that every cell was equally harmful and equipped with the ability to proliferate and create new tumors (**Figure 2.4**) [30].

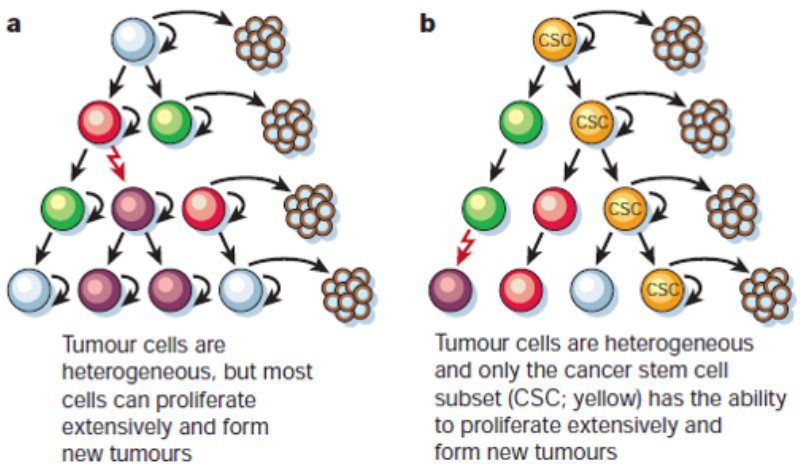

Figure 2.4: **(A)** An older tumor model which assumed that every cell was equally harmful and equipped with the ability to proliferate and create new tumors **(B)** The CSC theory treats tumor cells as a diverse population where only certain cells (the CSC cells) have the ability to proliferate extensively and potentially form new tumors [30].

If this were the case, then during treatment it would be expected that the tumor cells would begin to die off and the tumor would lose its ability to generate new cells causing the tumor to degenerate [30]. However, in many clinical cases, the tumor does not degenerate. It responds to treatment and then grows back. According to CSC theory this is because the treatment was successful at killing the majority of the tumor cells which are non-CSCs. However the CSCs are left untouched causing the tumor to first shrink in diameter as the non-CSCs are killed, but to grow back larger as the progeny of the CSCs continue to proliferate [30]. It has been shown that some tumor cells are resistant to radiation and chemotherapy [31, 32, 33, 34, 35, 36]. Current CSC concepts hypothesize that genetic diversity, epigenetics, and the tumor microenvironment all contribute to tumor cell heterogeneity and patient prognosis [37]. Additionally, CSC phenotypes based on cell markers are not exclusively positive or negative; they exist as a continuum of the particular cell marker. The goal of

the first half of this work is to characterize CSC populations using cancer cell lines as an acceptable model of study and to test if there is a correlation between breast CSCs and stiffness by (1) determining what percentage of the total population of cells do cancer stem-like cells make up in 3 different breast cell lines (MDA-MB-231, MCF-7, and MCF-10A) and (2) combining confocal microscopy with AFM to directly correlate CD44/CD24 fluorescence levels with stiffness at the single cell level. CSCs have been shown to correlate with the mesenchymal phenotype and follow some of the same pathways as the epithelial-to-mesenchymal transition. Since mesenchymal cells are softer than other cell types, it is hypothesized that the CSCs would be softer than the non-CSCs.

2.5 CSC identification and Breast Cancer

CSC identification began with leukemia stem cells [38]. Since then a number of experimental methods have been developed to identify CSCs in various cancer cell types such as clonogenic assays in semi-solid media, sphere-forming assays under floating cell culture conditions and with specific growth factors, and assays to investigate the differentiation potency of cells isolated from various differentiated cells. Additionally, cell surface markers detected by fluorescence-activated cell sorting (FACS) has been used to isolate possible CSCs.

It is hypothesized that breast CSCs originate from mammary multipotent stem cells due to genetic defects caused by damaging agents such as radiation that alter pathways governing self-renewal and differentiation [39]. A second theory suggests that breast CSCs develop from epithelial-mesenchymal transition (EMT) where cells that have undergone EMT can transform and behave similarly to normal and neoplastic stem cells. It has been determined that breast cancer cells possess a subpopulation of cells that are CD44+/CD24- and have been identified as CSCs [39, 40, 41]. These

cells have a higher probability for tumor regeneration in vivo and have been connected to poor patient prognosis [42]. Additionally, they are capable of self-renewal and differentiation and display increased resistance to radiation and chemotherapy. Breast CSCs are more invasive in vitro [42]. CD44+/CD24- cells possess a basal-like phenotype [43]. However, other publications state that it is CD44-/CD24+ rather than CD44+/CD24- that contributes to poor patient prognosis and one study in particular has connected CD24+ to invasive breast cancer [44]. High CD44+/CD24- expression represents a more basal/mesenchymal cell phenotype while CD44-/CD24+ expression represents a more luminal/epithelial cell phenotype [45].

2.6 Role of CD44 and CD24 in the Cell

Cell adhesion molecules are a family of proteins, in particular cell surface glycoproteins, which possess a large extracellular domain, a membrane spanning region, and an intracellular, cytoplasmic functional domain. These proteins are called adhesion molecules because they bond very strongly to specific ligands; however, the interaction is more advanced that just cell attachment and involves sensing the extracellular environment and passing that information along to nearby cells. These proteins are involved in cell-cell and cell-matrix interactions, cell migration, differentiation, cell signaling and gene transcription [46].

CD44 glycoproteins are members of the hyaluronate receptor family of cell adhesion molecules and are defined by their function rather than their structure. CD44 binds to ligands on the extracellular matrix (ECM). The most common isoform of CD44 has 363 amino acids and a molecular mass of 37kDa [46]. The main ligand of CD44 is hyaluronic acid. CD44's primary function is to maintain the 3D tissue/organ structure. Proliferating epithelia and cells in repair upregulate CD44 and hyaluronic acid [46].

Additionally, CD44 also plays a role in inflammation. CD44 has been shown to interact with another part of the ECM: osteopontin. It is hypothesized that the secretion of osteopontin and CD44 expression could cause migration and metastasis of tumor cells to specific sites. CD44 also interacts with HER2 cell surface protein, which when overexpressed in tumor cells is linked with poor prognosis for breast and ovarian cancer [46]. It has been shown that CD44 expression and CD44-mediated cell adhesion to hyaluronic acid were significantly reduced when a cell line was transfected with adenovirus 5E1A gene, which represses the synthesis of HER2 [47]. Tumor cell lines with higher CD44 concentrations have been shown to form more aggressive tumors in animal experiments [48, 49]. Altering the expression of CD44 in a tissue is likely to disrupt the normal epithelial-mesenchymal interactions and cause structural and functional disorganization which is a hallmark of cancer [46]. CD44 function in metastasis was first explored by Gunthert et.al. by transfecting plasmids expressing either the CD44s or CD44v isoform into non-metastatic rat pancreatic carcinoma cells. It was discovered that the CD44s had no effect on the tumor whereas the CD44v isoform promoted metastasis [46]. Later other groups demonstrated a correlation between CD44 expression and metastatic capability in human melanoma and lymphoma cell lines [46]; however in these studies it was the CD44s isoform that was associated with metastatic capability instead of the CD44v isoform suggesting that the isoform that is advantageous for tumor cell metastasis could be tissue/cell line specific. Since then, CD44 has been used as a diagnostic/prognostic marker in human tissue samples [46].

CD24 is a glycoprotein first identified in mice in 1978. Since CD24 has highly variable glycosylation, several ligands of CD24 have been determined but ligand specificity seems to be dependent on cellular context. It has a molecular weight ranging from 25 to 75 kDa whereas in normal epithelial cells, CD24 weighs 35-45 kDa [50]. CD24 is expressed in many different cell types including cancer cells and tends to

be expressed at higher levels in progenitor cells, metabolically active cells and terminally differentiated cells. CD24 function is not well understood; however, many immunological functions have been discovered when one studies the literature [51]. CD24 is overexpressed in many types of tumor tissues including breast cancer [51]. Additionally, human cancer stem cells seem to have a decreased expression of CD24 compared to their offspring [51]. CD24 has become an important marker for cancer diagnosis/prognosis. In breast cancer, CD24 expression is significantly higher in invasive carcinoma than in precancerous lesions [51]. CD24 cell surface and cytoplasmic expression have been correlated to poor prognosis, histology grades, tumor sizes, and lymph node positivity [51]. In experiments, small-interfering RNA silencing of tumor cell CD24 expression directly effected tumor cell proliferation and survival in tissue culture [51]. Additionally, a lack of CD24 is associated with invasiveness, metastasis, and cancer cell stemness [50]. Thus, there exists some contradiction in the literature over what exactly CD24 is associated with.

CD44 has been positively associated with stem cell-like characteristics whereas CD24 has been identified to relate to differential epithelial features [52].

2.7 Cell Mechanics

2.7.1 AFM and Stiffness of Cells

Lekka et.al [53] were the first to determine that there was a significant stiffness difference between tumor and benign cells using an AFM and human bladder cells. The tumor cells were significantly softer than benign cells with a stiffness of 0.56 ± 0.09 kPa compared to 2.10 ± 0.79 kPa. Li et. al [54], and Nikkhah [55] have shown that the same applies to breast cancer cells. Since then, it has also been determined that mesenchymal cell lines are considerably softer than other types of cell lines (basal, luminal, etc).

At the cellular level, tumor formation and progression is characterized by structural changes in the extracellular matrix (ECM) which can cause different mechanical responses [56, 57]. According to Plodinic et. al. [58], human breast biopsies display distinct stiffness profiles. Normal and benign tissues have a uniform stiffness profile with a single distinct peak whereas malignant tissue has a broad distribution due to tissue heterogeneity.

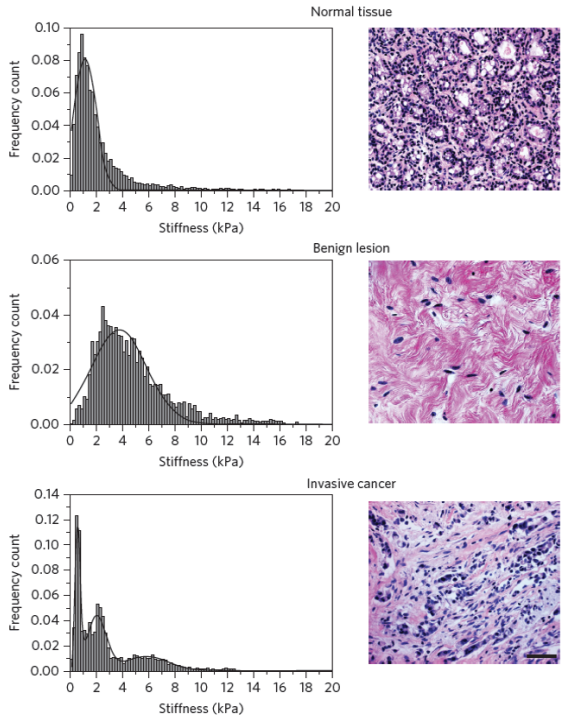

Figure 2.5: Stiffness Distribution of Breast Cancer Cells from Normal Tissue to Invasive Cancerous Tissue [58].

Additionally, migration and metastasis were correlated to low stiffness. Other studies in mice have shown that breast tumors are more stiff than the surrounding tissue [56]. However, single/cultured cancer cells are softer than healthy cells. The increase in elasticity and deformability is caused by alteratons in the ECM that have been linked to malignancy [58] [59].

2.7.2 Cell Mechanics in Breast Cancer

Human epithelial mammary cells can produce breast cancer stem cells (BCSCs) by epithelial to mesenchymal transition (EMT) induced by the RAS-MAPK pathway activation [60]. The transition to mesenchymal phenotype is detrimental because it allows cells to break free from the primary tumor site and metastasize at other distant locations. As the EMT is occuring, BCSCs will express the CD44+/CD24- cell surface marker phenotype [60].

Several pathways are implicated in the induction of EMT including: Wnt, TNF-$\propto$/NF-κB, Notch, Transforming growth factor-β(TGF-β), and Receptor Tyrosine kinase (RTK). CSCs take over these pathways for the goal of tumor formation. Below is a summary of how the deregulation of these pathways leads to EMT in cancer:

- Wnt signaling pathway: In breast cancer cells, Wnt signaling induces the expression of intracellular protein Axin 2 to stabilize the Snail, inducing EMT.
- TNF-$\propto$/NF-κB:TNF-$\propto$ activates NF-κB which induces the transcription of factors associated with EMT such as Snail, Slug, Twist, ZEB1, and ZEB2.
- Notch: The Notch pathway balances cell proliferation,differentiation, and apoptosis in normal cells. Notch signaling can be increased by TGF-β.

In summary, since CSCs can be produced by EMT and the mesenchymal phenotype is typically associated with a softer cell, this study wishes to determine if CSCs are softer than non-CSCs and could possibly correlate to a mesenchymal phenotype.

2.8 Cell Nuclei Properties

The cellular nucleus was first discovered in the 17th century by Antonie van Leeuwenhoek in salmon blood cells [61]. It is a highly compartmentalized organelle containing

chromatin, nucleoli, and smaller structures such as Cajal bodies and nuclear speckles [62]. Today, it is known that the nucleus is the site of the storage and organization of genetic material for the cell, DNA synthesis, DNA transcription, and RNA processing [62].Cancer biology has typically focused on the identification of oncogenes and tumor-suppressor genes. However, it has become apparent that in addition to these genetic factors, the biochemical factors and the microenvironment of the cell must be considered as well as the deformation of a large and stiff nucleus can be an obstacle during the passage through the dense interstitial space and narrow capillaries since it is the largest (occupying the largest fraction of cellular volume) and stiffest organelle in the cell [62]. Currently the most common and reliable diagnosis of cancer in tissue biopsies by pathologists relies on the presence of morphological changes in the nuclear structure of the cell (increased size, irregular shape, and nuclear organization) [63]. However, it is not well understood how these morphological changes correlate with functional changes in the nucleus.

Several studies have now reported altered nuclear envelope composition in various cancers [64, 65]. The structure and composition of the nucleus are important for cellular mechanics and function; these factors determine nuclear deformability and fragility as well as mechanotrasduction signaling [66]. A potential mechanism by which changes in the nucleus can contribute to cancer progression is that softer nuclei can facilitate cancer cell invasion thorugh the dense intersitial space where cells have to pass through regions smaller than the nuclear diameter [62]. Additionally, nuclear actin has been implicated in functions related to tumorigenesis such as DNA organization, orientation during replication, and RNA synthesis [62]. Experiments have revealed that the cellular nucleus exhibits elastic (nuclear lamina) and viscoelastic (nuclear interior) behavior and is roughly 2-10 times stiffer than the surrounding cytoplasm [62] and Young's modulus measurements range from 0.1 to 10 kPa based on experimental technique and conditions. The mechanical deformability of the nu-

cleus is mainly governed by the nuclear lamina and the nuclear interior according to micropipette aspiration experiments and computer modeling and varies according to mechanical load, cell type, and chromatin configuration [62]. The main contributors to nuclear stiffness are lamins A and C; loss of these lamins results in softer, deformable nuclei whereas increasing lamin A expression creates stiffer, less deformable nuclei [62].Additionally, chromatin can contribute to nuclear stiffness. Chromatin decondensation of embryonic stem cells causes softening of the nucleus [62]. The cell nucleus of human embryonic stem cells also changes during cell differentiation become 6 times stiffer and less fluid at the end of differentiation [62].

In conclusion, since lamin expression and chromatin organization have been shown to determine nuclear deformability, these changes could possibly alter nuclear rigidity. This lowered rigidity could help metastatic cancer cells migrate through tissues. Additionally, changes in chromatin organization could alter gene expression or DNA stability within the cancerous cell. Finally, it has been shown that lamin A expression influnces mesenchymal stem cell lineage differentiation [67] and that less metastatic cells have stiffer nuclei [68]. Thus, it is hypothesized in this dissertation that the CSC nuclei will be softer than their non-CSC nuclei counterparts.

Chapter 3

Experimental Techniques

3.1 AFM

3.1.1 History and Applications

The scanning tunneling microscope (STM), the precursor to the AFM, was invented by Gerd Binnig and Heinrich Rohrer in the early 1980s earning them the 1986 Nobel Prize for Physics [69]. The invention of the atomic force microscope and the first experimental implementation occurred in 1986 by Binning, Quate, and Gerber [69]. The AFM is one of the first instruments capable of imagining, measuring and manipulating matter at the nanoscale level. In cellular biology, AFM can be used to attempt to distinguish cancer cells and normal cells based on the mechanical properties of cells, and to evaluate interactions between a specific cell and its neighboring cells in a culture system. In this dissertation, the Asylum MFP-3D and the Agilent 5500 were used for the vast majority of the measurements so the description of AFM theory will be based towards those instruments. This chapter will provide relevant background information on collection and analyzing raw AFM data to extract quantitative mechanical properties.

3.1.2 Instrumentation and Calibration

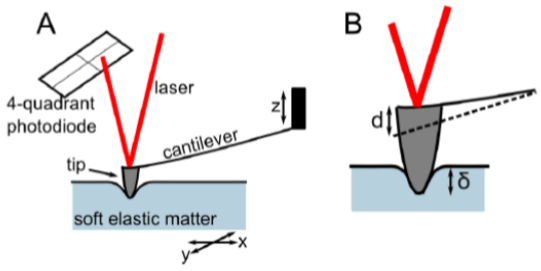

Figure 3.1: (A) A schematic of AFM instrumentation showing the photodiode and laser used to detect deflection signals and a cantilever with a tip/probe which moves in the z direction. (B) The magnitude of the deflection (d) and the magnitude of the indentation(δ) [70].

Figure 3.1 shows a basic schematic of AFM instrumentation. The indentation depth, δ, is given by:

$$\delta = z - d \tag{3.1}$$

where z is the relative distance of the cantilever base reported by the piezoelectric and d represents the cantilever deflection distance obtained from the inverse optical lever sensitivity, S_{OL}, and the change in voltage reported by the photodiode, ΔV, as shown in 3.2.

$$d = S_{OL}\Delta V \tag{3.2}$$

Then the force, F, experienced by the cantilever can be expressed as:

$$F = kd \tag{3.3}$$

where k is the spring constant of the cantilever.

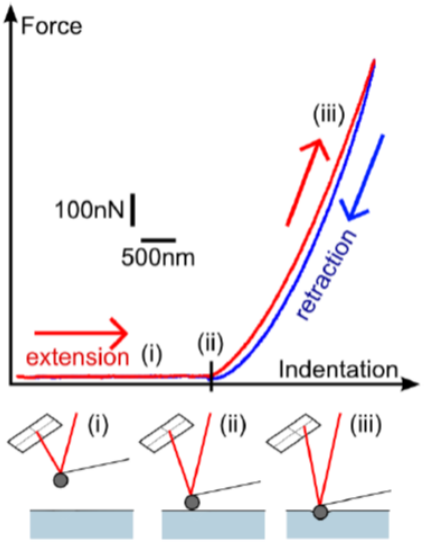

Figure 3.2: AFM Indentation and Retraction Curve [70]

Figure 3.2 shows an example of a force curve produced during measurement with AFM. The cantilever is lowered to the sample using piezoelectronics in the AFM head. For the Asylum-MFP-3D, there is a capacitive sensor inside the AFM head that reports the z-position of the cantilever. When the tip comes into contact with the sample, the cantilever bends, resulting in a deflection signal that will increase as the laser position on the photodiode is changed. When the tip comes off of the sample, the deflection signal will return back to the original baseline level unless there is adhesion between the tip and the sample. In an ideal elastic sample, the extension and retraction curves should perfectly overlay.

The AFM collects raw data as a voltage from the photodiode which must be translated into a usable quantity such as force. In order to collect accurate force data from the AFM, the cantilever spring constant, k, should be as accurate as possible and the OLS must be properly calibrated to reflect the actual deflection of the cantilever.

The simplest method for OLS calibration is to probe a rigid surface such as glass to determine a z-piezo versus photodiode voltage curve. Then assuming, $\delta z = \delta d$,

the inverse OLS can be calculated as the cantilever bending distance divided by the photodiode voltage. This process is dependent on the laser intensity and cantilever position so it must be recalculated each time the laser moves or the media in which the cantilever rests changes (measuring from air to liquid).

The most popular method for calibrating the spring constant is the thermal tuning method [71]. The cantilever is assumed to be a 1-D simple harmonic oscillator under weak thermal fluctuations. Then based on the equipartition theorem, the vibrational energy of each degree of freedom is given by:

$$\frac{1}{2}k_B T = \frac{1}{2}k < q^2 > \tag{3.4}$$

where k_B is the Boltzmann constant, T is the temperature, k is the cantilever spring constant, and q is the oscillator displacement [71]. The mean square oscillator displacement,$< q^2 >$, is determined by performing a frequency sweep and calculating the integral of the power spectrum of the first vibrational mode in the frequency domain [71]. Then the cantilever displacement can be related to the voltage from the photodiode by:

$$< q^2 >=< V^2 > S_{OL}^2 \kappa^2 \tag{3.5}$$

where S_{OL} is the inverse OLS and κ is the kappa factor which compensates for dynamic oscillations and the positioning of the laser on the cantilever. The power spectrum is fit to a Lorentzian:

$$P(f) = B + \frac{A_1 f_1}{(f^2 - f_1^2)^2 + (\frac{f f_1}{Q_1})^2} \tag{3.6}$$

to compute B, the background amplitude, the first mode amplitude peak A_1 (units:voltage), the resonance frequency, f_1, and the quality factor, Q_1, giving an area of [72]:

$$< V^2 >= \int_0^\infty P(f)df = \frac{\pi A_1 f_1 Q_1}{2} \tag{3.7}$$

Thus the final form of the spring constant derived from the thermal noise method is:

$$k = \frac{2k_B T}{\pi A_1 f_1 Q_1 S_{OL}^2 \kappa^2} \tag{3.8}$$

3.1.3 Analysis of Force-Indentation Data

There are several models that can be used to determine the Young's modulus from AFM force curves; however, the Hertz-Sneddon model is the model most widely used [73]. This model assumes that the sample is homogenous, isotropic, and infinitely thick [74].

The contact point can be visually determined as shown in Appendix B. Then the Young's Modulus (E) can be determined by:

$$F(\delta) = \frac{E}{(1-v^2)}\lambda(\delta) \tag{3.9}$$

where F is the force, δ is the indentation depth, and λ is a function that models the shape of the indenter with the units of distance squared. R is the tip radius for which $R >> \delta$. For parabolic (Hertz model) and conical (Sneddon model) indenters, λ is a power law function with base δ and exponents of $\frac{3}{2}$ and 2 [75]. The tip shapes utilized in the experiments for this dissertation are parabolic(Hertz model), spherocone, and conical(Sneddon model) so the function used to determine the Young's modulus (E) of each tip shape is given below [76, 77]:

$$F_{Hertz} = \frac{4}{3}\frac{E}{(1-v^2)}\sqrt{R\delta^3} \tag{3.10}$$

$$F_{Sneddon} = \frac{2\delta^2}{\pi cot\theta} \frac{E}{(1-v^2)} \tag{3.11}$$

In the spherical region [78]:

$$F_{Spherocone}(a \leq b_{SC}) = \frac{E}{1-v^2}[\frac{1}{2}(a^2+R^2)ln(\frac{R+a}{R-a}) - aR] \tag{3.12}$$

And in the conical region [78]:

$$F_{Spherocone}(a > b_{SC}) = \frac{E}{1-v^2}[a^2 \cot\theta \cos^{-1}(\frac{b}{a}) + b\cot\theta\sqrt{a^2-b^2} - aR$$
$$+\sqrt{(R^2-b^2)(a^2-b^2)} + a^2 \ln(\frac{R+a}{\sqrt{R^2-b^2}+\sqrt{a^2-b^2}}) - \frac{R^2}{2}\ln(\frac{a^2R^2-(b^2-\sqrt{(R^2-b^2)(a^2-b^2)})^2}{b^2(R+a^2)})] \tag{3.13}$$

For the above equations, a is the contact radius (such that 0≤r≤1) and $b = R\,cos\,\theta$ where b is the transition point between the cone and sphere.

3.1.4 AFM Applications in Cell Mechanics

Cell mechanics can provide information on the physiological or pathological state of a cell during differentiation, aging, and the onset of disease. The extracellular matrix (ECM) is the region where different types of cells are embedded in complex organisms. The ECM is composed of water, proteins, and polysaccharides and has a unique composition, topography, and mechanics during tissue development [79]. It regulates the physiological activities of the cell and helps the cell withstand stress [80, 81]. Cells can sense the mechanical properties of the ECM and translate these mechanical signals into signals that regulate gene and protein expression in cells affecting adhesion, migration, proliferation, and differentiation of cells [81, 82]. On the other hand, the ECM stiffness can guide stem cell differentiation [83]. For example, ECM with a Young's modulus of the brain (0.1-1 kPa) can guide a stem cell to differentiate into a neuron [84]. Cellular mechanics can be quantified by many different methods such

as microfluidics [85], optical tweezers [86] and AFM [73]; however, AFM is the most popular method [87, 88] because it has nanometer resolution, can work on suspended and adherent cells, and can work in liquid conditions [87, 88].

In nanomechanics, AFM has been used to monitor cellular processes such as migration and division [89], cytoskeletal reorganization [90] and exocytosis [91]. For cancer in particular, changes and alterations of cell properties can identify pathological states like cell deformability, cell adhesion, and cell mechanics [92, 93, 94, 95]. In 1999, Lekka et. al. [53], pioneered AFM use in cancer by showing that cell mechanics can be a key factor in cancer diagnosis due to the identification of specific mechanical phenotypes. They determined that normal bladder cells were one order of magnitude stiffer than cancerous bladder cells. Later many other groups studied cancer and non-cancer cells in various tissue types and determined that in general cancer cells are softer than normal cells [96] due to changes in cytoskeleton structure [96]. Additionally, malignant cells are more deformable and 33% less adhesive than normal cells [96]. Li et. al. [54] measured the Young's Modulus of the benign human breast cell line, MCF-10A, and the malignant breast cell line, MCF-7, and correlate the cell mechanics with the cell cytoskeleton. AFM imaging combined with actin-stained fluorescence showed that there were more actin filaments in MCF-10A than MCF-7 [54]. Additionally, the MCF-10A actin filaments had a more organized network structure whereas the MCF-7 possessed disorganized actin filament structure [54]. Surrounding environmental conditions can also affect cell mechanics; Nikkhah et. al. determined that the Young's modulus of normal and cancer cells decreased up to 18% when growth serum was reduced from 10% to 5%.

3.2 Fluorescence and Confocal Microscopy

3.2.1 Fluorescence

The process of fluorescence involves the absorption of a photon by a fluorophore and the emission of this light at another wavelength [97]. Some energy is lost in this process so the emitted photon has less energy than the absorbed photon [97]. Light with a short wavelength (toward the blue) has higher energy than light with a long wavelength (toward the red) [97]. Therefore, light emitted from a fluorophore usually has a longer wavelength than that of the absorbed (excitation) light. This change is called the Stokes shift [97]. Large Stokes shifts are generally desirable because the emitted light from the fluorescent tag can be filtered out more easily from the excitation light [97]. The goal of fluorescent microscopy then is to separate the emitted light from the excited light [97].

3.2.2 Confocal Microscopy

The principle of confocal imaging was patented in 1957 by Marvin Minsky and aimed to overcome some of the limitations of traditional wide-field fluorescence microscopes [98]. In a wide-field fluorescence microscope, the entire specimen is flooded evenly in light from a light source. All parts of the specimen in the optical path are excited at the same time and the resulting fluorescence is detected by a camera including a large unfocused background part. In contrast, a confocal microscope uses point illumination and a pinhole in an optically conjugate plane in front of the detector to eliminate out-of-focus signal. As only light produced by fluorescence very close to the focal plane can be detected, the image's optical resolution, particularly in the sample depth direction, is much better than that of wide-field microscopes. However, as much of the light from sample fluorescence is blocked at the pinhole, this increased resolution is at the cost of decreased signal intensity so long exposures are often required.

To offset this drop in signal after the pinhole, the light intensity is detected by a sensitive detector, usually a photomultiplier tube (PMT) or avalanche photodiode, transforming the light signal into an electrical one that is recorded by a computer [99]. Since only one point in the sample is illuminated at a time, 2D or 3D imaging requires scanning over a square pattern of parallel scanning lines in the specimen. The beam is scanned across the sample in the horizontal plane and the scan speed can be varied. Slower scans provide a better signal-to-noise ratio, resulting in better contrast and higher resolution. The achievable thickness of the focal plane is defined mostly by the wavelength of the used light divided by the numerical aperture of the objective lens squared, but also by the optical properties of the specimen. Since optical sectioning is possible with confocal microscopes, these types of microscopes particularly good at 3D imaging and surface profiling for thicker samples ($\geq$50 μm) samples since the out-of focus blur from each image section is removed allowing for the visualization and measuring of interesting sample features [100]. Successive slices make up a 'z-stack' which can either be processed by certain software to create a 3D image, or it is merged into a 2D stack [101]. Confocal microscopy provides the capacity for direct, noninvasive, serial optical sectioning of intact, living specimens with a minimum of sample preparation as well as a marginal improvement in lateral resolution [99]. There are 4 modes of confocal imaging [100] but since the CLSM was used for this dissertation, its technique, strengths, and weaknesses will be discussed here.

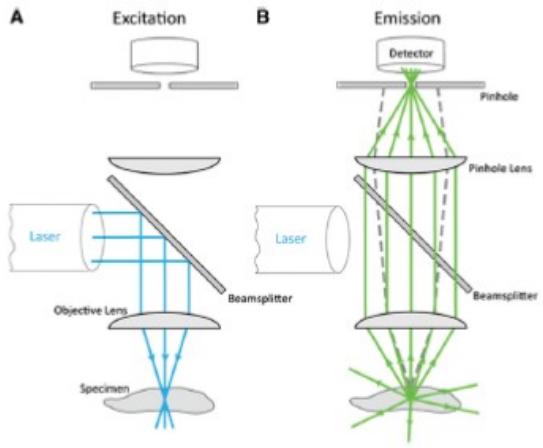

Figure 3.3: The Optical Principle of a CLSM [100]

Light from a laser beam is focused down to a small spot in the specimen, causing fluorescence in the entire cone of illumination (**Figure 3.3**). Lasers are required because they produce an intense beam that can be readily focused down to a tiny spot that is required for the CLSM. Fluorescence emission from the in-focus plane is imaged through a pinhole onto a detector, which measures the fluorescence intensity for this one spot and correlates to 1 pixel of the image. Fluorescence from out-of-focus planes is blocked by the pinhole. The focused spot is scanned back and forth across the specimen to generate an image pixel by pixel. To form a 3D data set (z stack), the focus can then be changed and another image generated at the new focal depth. Then successive images are collected at various focus depths to generate a 3D image stack [100].

The fluorescence from the sample is collected by the objective lens and focused through a confocal pinhole, onto a PMT. The PMT has a light-sensitive photocathode that converts photons of light that hit the detector into photoelectrons that are then amplified by a series of diodes. The analog PMT signal is then digitized to a gray level (usually 12 bit, so a value between 0 and 4095) and stored by a computer along with the precise x, y location of the focal point. PMTs are not very sensitive; they only

have a quantum efficiency (QE) of 20% but they are very good amplifiers because each photon signal that is detected is amplified thousands of times [100]. Slower scan speeds will result in better signal to noise ratio because each pixel intensity will be integrated longer which increases signal and reduces noise; however, photobleaching of the fluorophore will also increase. In the CLSM, the pinhole size can be adjusted to match the resolution of the objective lens and the color of light. In addition, the pinhole can be made larger to image light-sensitive specimens such as living cells, or the pinhole can be closed down to a smaller size for bright, stable samples when maximal resolution and 3D-sectioning ability are required. For multicolor imaging, the CLSM can also have 23 detectors collecting different colors sequentially [100]. The main weaknesses of the CLSM are speed and sensitivity. For live-cell imaging, the CLSM causes a lot of phototoxicity because it relies on a highly temporally and spatially localized laser spot; these effects can be minimized by using lower laser powers, higher scan speeds, and line averaging [100].

3.3 Salt Fractionation

The concept of salt fractionation, or salting out, is a process where the solubility of a nonelectrolyte substance in water decreases with increasing salt concentration [102]. The exact mechanism of salt fractionation is still debated [103]. A very simple model states that salt fractionation is caused by dissolved anions of high charge density releasing the sample through a combination of electronic repulsion [104]and enhancement of the hydrophobic effect [105]. In pure water, the hydrophobic effect causes the solute to aggregate and minimize the entropic penalty associated with the highly-ordered structure at the solute-water interface [106]. In the presence of additional salt, the surface contacts are more ordered and have an even larger entropic penalty creating a state that is unfavorable energetically and thus causes the solute

to leave the aqueous phase [107]. Sanders [108] described a method to quantitatively recover chromatin from cells using a salt extraction method. Washing of MNase-treated nuclei with increasing salt concentrations isolates chromatin fractions with different genome-wide profiles: a low-salt fraction of highly accessible chromatin, a high salt fraction containing the majority of the chromatin, and an insoluble fraction of chromatin derived from transcribed regions of the genome. This technique will be utilized for experiments in Chapter 4 to isolate and quantify the DNA of two esophageal cell lines.

3.4 Spectrophotometry

To identify the quantity of DNA in each salt fraction, a spectrophotometer was used. A spectrophotometer is a device that measures absorbed light intensity as a function of wavelength. The first spectrophotometer was created by Arnold O. Beckman in 1940 [109]. A spectrophotometer contains five basic components: a light source, a monochromator, a sample holder, a detector, and an interpreter [110].

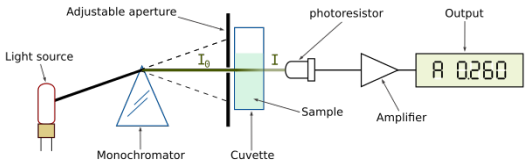

Figure 3.4: Essential Parts of a Spectrophotometer [111]

To make a measurement, a light source with a known intensity(I_o) is passed through a cuvette containing the sample. The light intensity (I) is measured after passing though the sample and using Beer-Lambert's law, A=$\log\frac{I}{I_o}$=ϵlc, the absorbance (A) of the sample can be determined where ϵ is the extinction coefficient of the sample in $M^{-1}cm^{-1}$, l is the path length of the cuvette in centimeters and c is the concentration of the sample in M. The are two classes of spectrophotometers:

single beam and double beam. A double beam spectrophotometer compares the light intensity between two separate light paths (the reference path and the test sample path) whereas a single beam spectrophotometer compares the light intensity of the sample before and after a test sample is inserted. Double beam spectrophotometers are considered to provide a more stable light intensity reading and therefore a more accurate absorbance reading [112]. In this dissertation, the Cary 300 UV-Vis, a double beam spectrophotometer, was used for the vast majority of the measurements so the description of spectrophotometry will be based towards this instrument. Additionally, for this dissertation, a quartz cuvette was used with a path length of 1 cm.

To determine the absorbance of a DNA sample, the absorbance of the sample is measured at 260 nm since this is where DNA maximally absorbs light. Once the absorbance of the sample has been determined, the DNA quantity of the sample can be determined by the following formula: DNA yield (g) = $A_{260}\times$ dilution factor $\times$ 50 μg/ml $\times$ total sample volume (ml) where the 50 μg/ml represents the standard extinction coefficient of double stranded DNA when the Beer-Lambert law is solved for a cuvette path length of 1 cm where ϵ=0.020 $(\mu\text{g/ml})\,\text{cm}^{-1}$ and A=1 [113].

Despite purification techniques, it is common for nucleic acid samples to be contaminated with other organic compounds or proteins. Thus, the second benefit of using a spectrophotometer for sample analysis and quantification is that the purity of the sample can be determined using the A260/A280 ratio of the sample since proteins (particularly aromatic amino acids) absorb at 280 nm [114]. The ratio of pure DNA is considered to be 1.8 and the ratio of pure RNA is considered to be 2.0 [114]. It takes a relatively large amount of protein contamination to affect the A_{260}/A_{280} ratio in a nucleic acid solution due to the much higher mass attenuation coefficient nucleic acids have at 260 nm and 280 nm, compared to that of proteins. Because of this, protein contributes little error to DNA quantity estimation on a spectrophotometer

[114]. In this dissertation, the A260/A280 ratios were determined to assess the purity of the DNA sample.

Chapter 4

An Analysis and DNA Quantification of the Supernatant Fraction Previously Discarded in Salt Fractionation Studies

This chapter details experiments to identify the reason for DNA unaccounted for in salt fractionation experiments, the process used to quantify the total DNA in two cell lines (CP-D and EPC2), and the subsequent analysis of the nuclei of cancer and non-cancer cells. The CP-D cell line is a hypotetraploid, cancerous, human esophageal cell line with high grade dysplasia and exhibits a large nucleus to cytoplasm ratio. EPC2 is a normal human esophageal cell line. [115]. 3-D fluorescent imaging was performed by Nethmi Ariyasinghe and Bo Faust and analyzed by Nethmi Ariyasinghe. Cell culture was performed by Nethmi Ariyasinghe and Bryant L. Doss, also acknowledging support from Nikita Satapathy. The DNA quantification experiments were conducted by Nethmi Ariyasinghe. The protocol for extracting the cellular chromatin was developed by Steve Henikoff and modified by Subahadip Senapathy [116, 117]. The

protocol for salt fractionation was previously discussed in Chapter 2 of this thesis. Gel electrophoresis experiments were performed by Nethmi Ariyasinghe and Brendon Sullivan. Chromatin imaging using AFM and analysis was performed by Nethmi Ariyasinghe. DNA and RNA sequence analysis was performed by JongOne Im.

4.1 Introduction

In 1978, Marilyn Sanders devised a method to extract the chromatin from rat liver nuclei and described three types of nucleosome packing interactions based on increasing NaCl concentration [108], a technique later described as salt fractionation. In summary, salt fractionation is a process where increasing salt concentrations are added to a sample of chromatin extracted from nuclei to release nucleosomes from the sample. She used a diphenylamine procedure [118] to measure the DNA quantity present in each fraction of increasing salt concentration (0.2M, 0.3M, 0.4M and 0.6M NaCl) as well as a fraction without any added salt, the S_0 fraction. The diphenylamine procedure used to measure the DNA quantity is a technique where DNA is heated to 100°C for a few minutes with acetic acid, sulfuric acid, and diphenylamine first described by Dische [119] and modified by Burton. Burton [118] additionally suggested mixing the samples with perchloric acid as well. Protein contamination would result in turbidity and report higher concentrations of DNA [120]. The underlying principle for the basis of estimating DNA using diphenylamine is that the reaction of diphenylamine with deoxyribose sugar produces a blue-colored compound. When DNA is boiled under extremely acidic conditions it causes depurination of the DNA followed by dehydration of deoxyribose sugar into a highly reactive ω-hydroxylevulinylaldehyde which reacts with diphenylamine to produce a blue-colored complex that absorbs at 595 nm. In her publication, Sanders claims that no DNA is released in the S_0 fraction, 20% (of the total DNA) is released at 0.2M, 60% at 0.3M, and 100% at 0.4M. However, it

has been stated in previous publications that quantifying DNA concentrations with diphenylamine is unreliable for small amounts of DNA due to the large amount of color produced by the diphenylamine blank [120]. Additionally there can be non-specific color from the sulfuric acid interacting with other biological material [120]. Due to Sander's claim that there was no DNA in the supernatant (S_0) fraction, several subsequent publications that have studied DNA and chromatin have also not looked at this fraction.

It was determined that the salt fractionation technique created by Marilyn Sanders in 1978 left about 30% of the total DNA quantity unaccounted for in epigentic experiments conducted to determine how chromatin structure is different in cancer nuclei compared to non-cancer nuclei. The goal of this project then sought to (1) determine the reason for DNA unaccounted for in salt fractionation experiments, (2) quantify the relative amount of DNA in each cell line using spectrophotometry, and (3) characterize the differences in the nuclei of cancerous and non-cancerous cell lines in regards to nuclear size and shape, chromocenters, nucleoli size and quantity, and nuclear speckle volume.

4.2 Materials and Methods

4.2.1 Cell Culture

The esophageal cell lines EPC2 and CP-D were cultured in Keratinocyte-SFM (Life Technologies) media with the provided supplements [121]. The cancerous colon cell line RKO was cultured in EMEM with 10% FBS [121]. All growth media also contained 1x penicillin-streptomycin [121].

4.2.2 3-D Fluorescence Imaging

3-D fluorescence imaging with EDTA was performed in HBSS with 5mM EDTA, 25 mM HEPES, no CaCl2 and no MgCl2 on two cell lines (CP-D and EPC-2 as esophageal cancer and normal esophageal cells) both with and without TS-A (1μM, 24 hr); nuclei were stained with DAPI dye. Cells were incubated immediately before measuring at a concentration of 200 nM in measuring buffer for 20 minutes and then washed thoroughly with the measuring buffer. 3-D confocal imaging was performed on fixed cells at room temperature using the Leica SP8.

4.2.3 Chromatin Extraction, Salt Fractionation, and DNA Extraction

A cancerous (CPD) and non-cancerous (EPC2) esophageal cell line were cultured in 2-D monolayers. Cells were harvested and washed with 1xPBS at 1000 RPM for 5 minutes at 4°C followed by a wash with 1XPBS containing 0.1% tween-20, a detergent that helps disrupt the cellular membrane. Next cells were lysed with mild NP-40 detergent (which can break the cytoplasmic membrane but not the nuclear membrane) in 0.5mM PMSF to release nuclei. PMSF blocks serine proteases such as trypsin and chymotrypsin. After mixing the cells gently, they were set on ice for 2 minutes and then spun down at 4°C at 1000 RPM for 10 minutes. The supernatant was discarded and the pellet was washed with 5 ml of TM2 buffer with 0.5 PMSF and centrifuged again at 4°C at 1000 RPM for 10 minutes. Then the pellet was suspended in 1 ml of 0.1 TE with 0.5 mM PMSF and incubated at 37°C for 5 minutes. Washed nuclei are subjected to an MNase digestion to fractionate the chromatin as seen in **Figure 4.1**. Successive incubation with buffers containing increasing salt concentrations differentially solubilized the chromatin (salt fractionation). RNase and proteinase are used to separate the RNA and protein in the chromatin structure

from DNA. Then a phenol chloroform and ethyl ether extraction are used to isolate and purify the DNA.

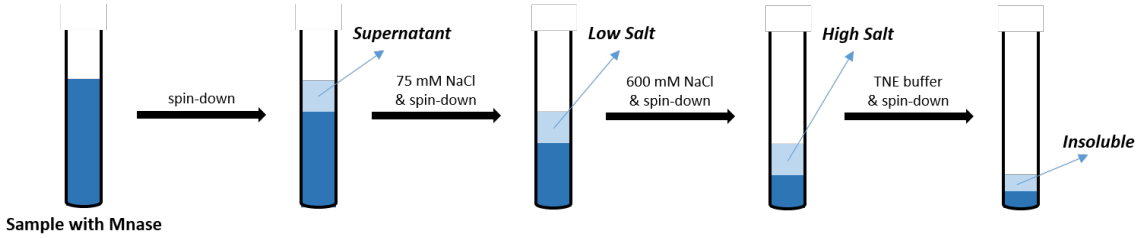

Figure 4.1: Extraction of Chromatin Using Salt Fractionation

4.2.4 Spectrophotometry

A Cary 300 UV-Vis (Simple Reads) was used to quantify the amount of DNA in the supernatant fraction, low, high, and insoluble salt buffers for each cell line. The purity of the DNA was verified using the A_{260}/A_{280} ratio of the sample. The quantity of DNA in each sample was calculated using the A_{260} value.

4.2.5 AFM Imaging of Chromatin

All chromatin samples were cross-linked with 0.5% gluteraldehyde for 15 minutes and then diluted in 0.1 TE buffer before imaging. Samples were placed on APTES-modified mica. After 5 minutes, the mica surface was washed with water and dried using nitrogen gas before imaging. AFM topographic images were taken in tapping mode using an Agilent 5500 AFM instrument. The cantilever used for topographic imaging had a length of 225 μm, width 32 μm, and a thickness of 2.5 μm and a resonant frequency between 50-70 kHz (typically 65 kHz)(AppNano SPM Probe: FORT model). Images were taken with a 4-6% drive. Images were processed using Gwyddion software. First each image was leveled using a three point level. Then the rows of each image were aligned using a 2 degree polynomial and horizontal scarring was corrected.

4.2.6 Data Analysis

3-D confocal data was analyzed using NucleusJ in ImageJ [122]. All images were converted to 8-bit and individual cells were isolated in the stack making sure that the first and last slide of each stack was blank. The contrast of each stack was enhanced, background noise was removed, and the entire stack was smoothed before running the Nuclear Segmentation and Analysis portion of the program. For chromocenter analysis, images were further filtered by applying a Gaussian Blur filter where σ=1. For nuclear speckle characterization, each slice in the stack was analyzed to determine the total volume of the dark regions. Then the nucleoli volume was subtracted from the total volume of the dark regions resulting in only the volume of the speckle regions.

4.3 Results and Discussion

In 1978, Marilyn Sanders created the salt fractionation technique to isolate the chromatin of rat liver nuclei and gain insight into the nucleosome packing interactions of the extracted chromatin. In her study, she claims that there is no release of DNA before the adding of NaCl (the S_0 fraction). Her technique has been subsequently used in a number of studies to gain insight into the chromatin of various species [117]. However, none of these studies have ever isolated and studied the S_0 fraction presumably assuming that it contained no DNA as Sanders stated in her publication. We began our study in a similar fashion using salt fractionation to isolate the chromatin of a cancerous and non-cancerous cell line and study the differences between the two cell lines to gain more information into the differences of cancer and non-cancer on a genotypic level. Additionally, as Sanders did, we varied the Mnase digestion time to determine if it would have any effect on how much DNA was extracted from each fraction. As seen in **Figure 4.2**, there is no effect of Mnase digestion time on the low salt and high salt samples verifying the results of Sanders in 1978; approximately equal

amounts of chromatin are extracted at the different Mnase digestion times demonstrating that the crosslinks that prevent chromatin from exiting the nuclear pore are electrostatic in nature [108]. However, what we surprisingly discovered is that the fraction of the total DNA that ends up in the low and high salt fractions for both cancer and non-cancer cell lines is relatively the same (roughly making up 40-70% of the total DNA) meaning that at least 30% of the total DNA is unaccounted for in these fractions.

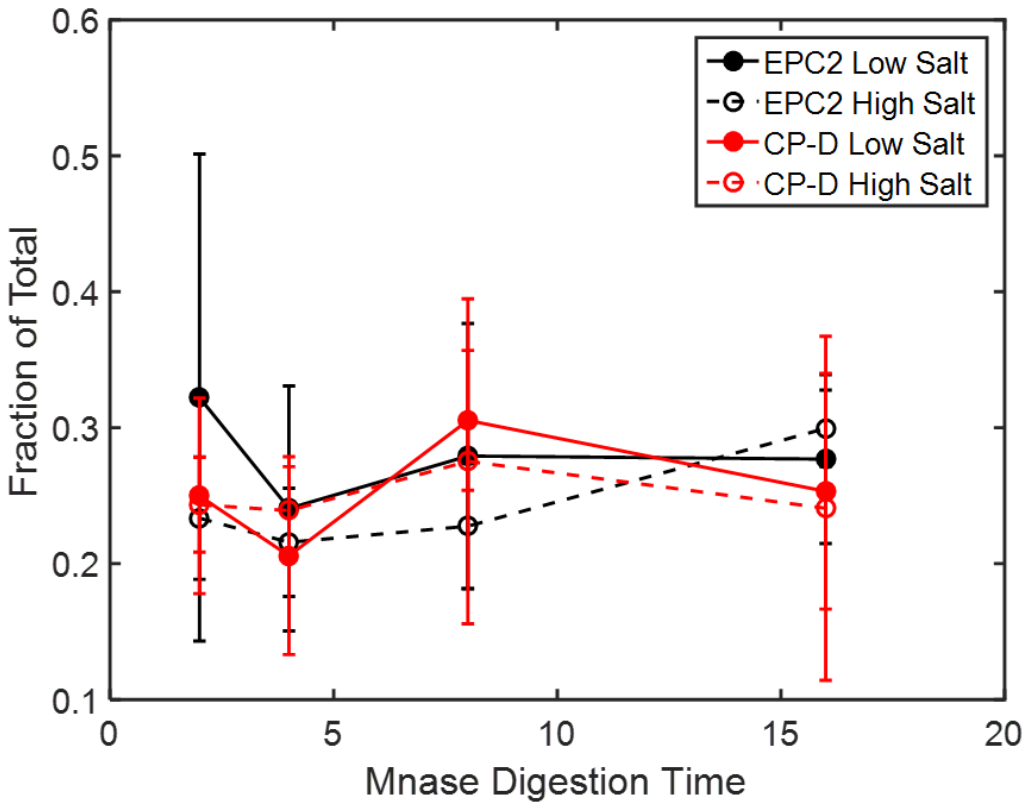

Figure 4.2: Total DNA fraction as a function of Mnase digestion time for two esophageal cell lines: CP-D (cancerous) and EPC2 (non-cancerous).

Thus the goal of this work was to identify the reason for DNA unaccounted for in salt fractionation experiments as well as to characterize this DNA.

In addition to the two low salt and high salt fractions previously collected, a

supernatant fraction was also collected before the addition of any salt to the sample in 0.1 TE buffer (the S_0 from the Sanders study) as well as an insoluble fraction collected after the high salt fraction characterized by an even higher concentration of salt (TE buffer with EDTA). We used gel electrophoresis to test these samples to determine if the supernatant fraction and the insoluble fraction contain any DNA (see Appendix).

Then based on the ploidy of each individual cell line (CP-D: hypotetraploid(<4n) [115], RKO: tetraploid(4n), and EPC2: diploid(2n) [115]), the amount of DNA per cell was calculated as follows for each cell line:

- **tetraploid**: $3.2\text{x}10^{9}$ basepairs x 4 x 650 Da/basepair x $1.66\text{x}10^{-12}$ pg/Da x $1\text{x}10^{-6}$ μg/pg = $1.30\text{x}10^{-5}$ μg/cell
- **diploid**: $3.2\text{x}10^{9}$ basepairs x 2 x 650 Da/basepair x $1.66\text{x}10^{-12}$ pg/Da x $1\text{x}10^{-6}$ μg/pg = $6.91\text{x}10^{-6}$ μg/cell

The CP-D cell line was treated as tetraploid to simplify calculations when determining the amount of DNA per cell.

It was determined that the automated cell counter was unable to detect the small RKO cells accurately for a perfect count (**Figure 4.3**); therefore, all cells were counted manually to ensure a more accurate cell count.

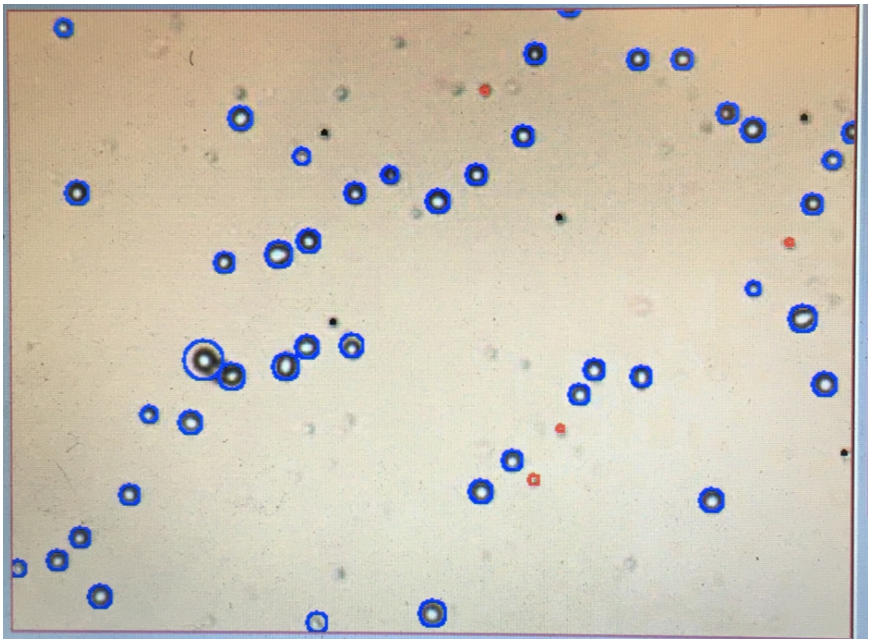

Figure 4.3: Image of the automated cell counter results for RKO cells. Live cells are shown in blue, dead cells are shown in red and black cells were excluded from the count. Additionally, cells not focused on the viewing plane were not included in the automated count.

Cell Line/Trial	DNA per cell (µg)(x10^{-5})	Supernantant Fraction (µg)	Low Salt Fraction (µg)	High Salt Fraction (µg)	Insoluable Fraction (µg)	Total Quantity Extracted (µg)	Quantity of Cells Counted (millions)	Expected DNA Quantity (µg)	Percent Discrepancy (%)
CP-D Trial 1	1.30	90	17	40	22	169	9.5	131	29
CP-D Trial 2	1.30	82	20	23	23	148	15	198	25
CP-D Trial 3	1.30	33	60	91	36	220	30	396	44
CP-D Trial 4	1.30	55	30	27	11	123	15	198	38
EPC-2 Trial 1	0.69	31	21	15	6	73	11.4	79	8
EPC-2 Trial 2	0.69	20	6	8	10	44	3.2	22	100
EPC-2 Trial 3	0.69	36	10	17	12	75	30	207	64
EPC-2 Trial 4	0.69	77	24	26	9	136	30	207	34

Table 4.1: The total amount of DNA obtained from each salt fraction shown for every CP-D and EPC2 trial performed along with the expected quantity of DNA expected based on the total number of cells. RKO results can be found in the appendix.

As shown in **Table 4.1**, for each trial conducted, the quantity of DNA for each

fraction was determined and compared to the expected quantity of DNA based on the total number of cells manually counted for each trial. On average (percent discrepancy), about 36% of the total DNA sample is lost due to purification methods. Additional results for the DNA quantification for the RKO cell line can be found in the appendix.

Finally, a more complete picture of the DNA quantity found in each fraction emerged as shown in **Figure 4.4**. A large portion of the genome is not isolated in either the low or high salt fraction but exists in the supernatant fraction making up around 30-40% of the total DNA; this result is further verified by DNA sequencing of the genome **Figure 4.4b**. Additionally, the CP-D line shows a wider variation of DNA distributions in each fraction when compared to the EPC2 cell line.

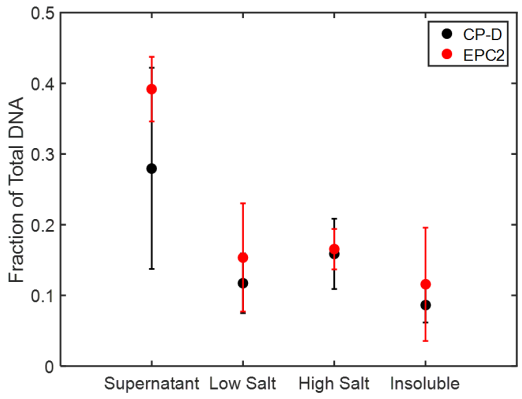

(a)

Total Number of Fragments					
		4 min		16 min	
		counts	% ratio	counts	% ratio
CPD	Su	65,895,669	33	62,734,560	39
	LS	64,742,791	33	45,710,047	28
	HS	40,230,175	20	33,931,325	21
	In	26,127,709	13	18,882,045	12
EPC2	Su	73,595,139	43	137,123,631	52
	LS	37,523,884	22	37,759,719	14
	HS	41,543,253	24	69,752,977	27
	In	17,202,778	10	17,185,586	7

(b)

Figure 4.4: **(a)** Total DNA fraction as a function of salt fractionation. **(b)** DNA sequencing results for the CP-D and EPC2 cell line at 4 min and 16 mins.

After identifying the reason for DNA unaccounted for in salt fractionation experiments and quantifying the amount of DNA for each cell line, further work was done to characterize the supernatant fractions and compare them with previous work done by Subhadip Senapathy. AFM images of the chromatin from the supernatant fraction at the 2, 4, 8, and 16 minute Mnase digestion time were taken for the EPC2

and CP-D cell lines (**Figure 4.5** and **Figure 4.6**).

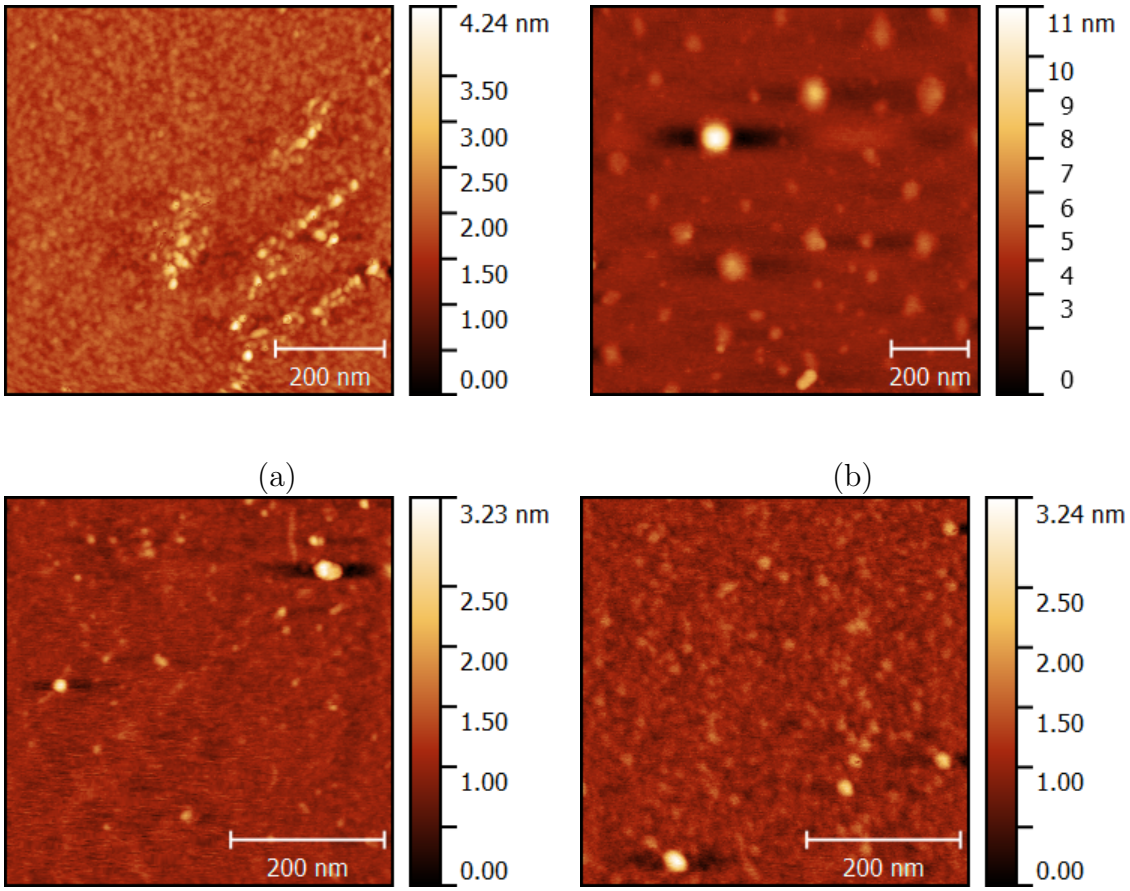

Figure 4.5: AFM Images of EPC2 supernatant fractions at different Mnase digest times: **(a)** 2 min, **(b)** 4 min, **(c)** 8 min, and **(d)** 16 min.

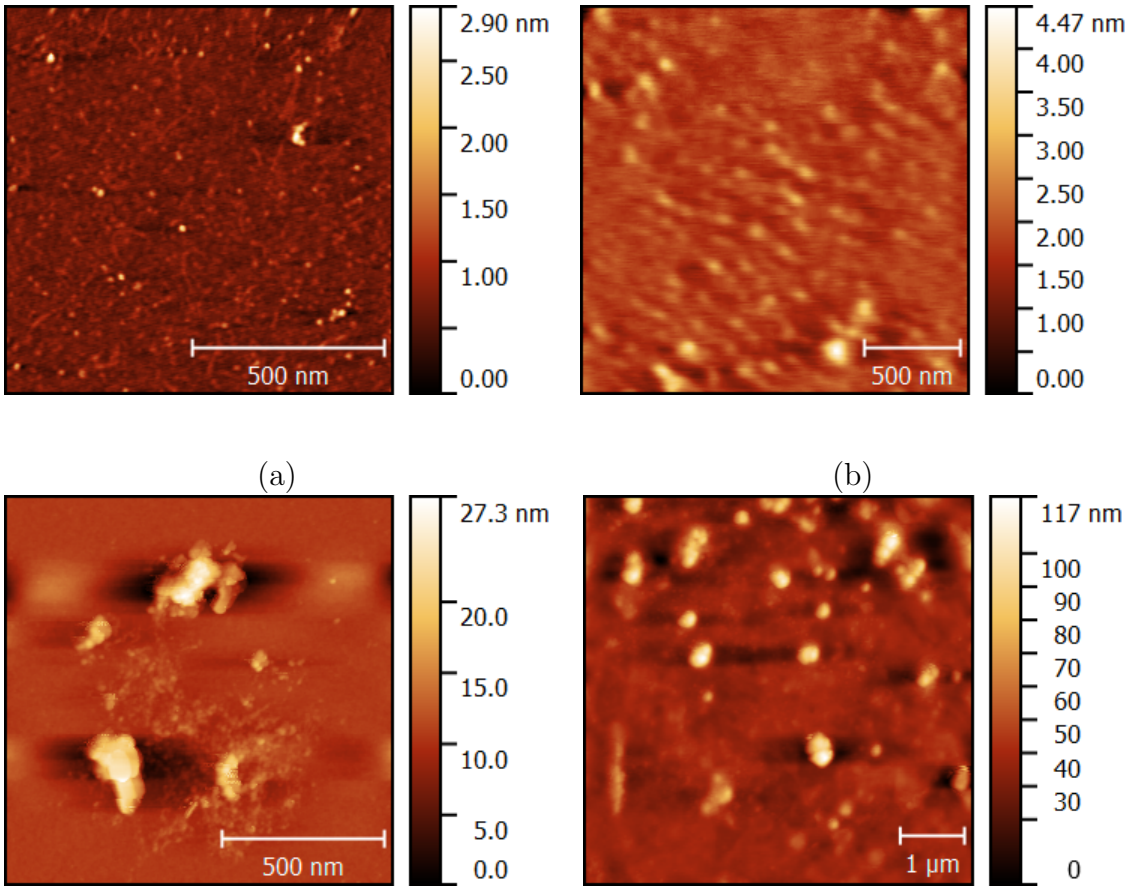

Figure 4.6: AFM Images of CP-D Supernatant fractions at different Mnase digest times: **(a)** 2 min, **(b)** 4 min, **(c)** 8 min, and **(d)** 16 min.

These figures show that for the EPC2 cell line, at 2 mins, the chromatin is digested into single nucleosomes that seem to form arrays. At 4 mins, 8 min and 16 min, the chromatin exists as individual nucleosomes. For the CP-D cell line, at 2 mins, the chromatin is digested into single nucleosomes. At 4 mins, 8 min and 16 min, the chromatin exists as a combination of single nucleosomes and nucleosome clumps.

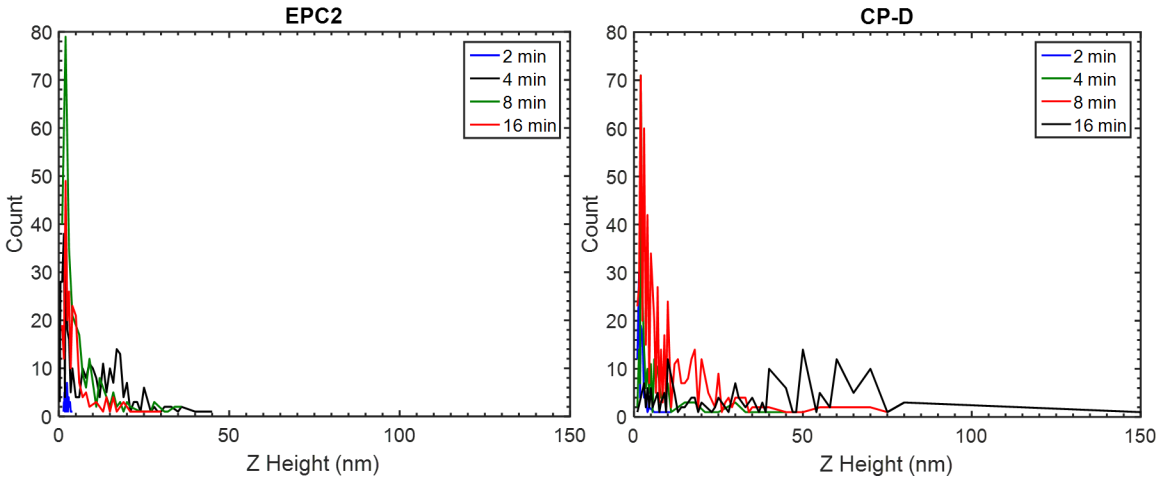

(a) (b)

Figure 4.7: The nucleosome height distributions of the chromatin from AFM images of the supernatant fraction for **(a)** EPC2 **(b)** CP-D

As seen in **Figure 4.7**, the majority of the chromatin exists as single nucleosomes for both the EPC and the CP-D cell lines. However, there is a larger distribution of nucleosome heights in the CP-D suggesting that this cell line contains more undigested chromatin than the EPC2.

Next, work was undertaken to identify and quantify the differences in the nuclei of a cancerous (CP-D) and non-cancerous (EPC2) cell line. Images of nuclei stained with DAPI were taken using 3D confocal imaging and quantified using NucleusJ in ImageJ [122].

	Nuclear Volume (μm^3)	**Flatness** (length of intermediate axis/length of shortest axis)	**Elongation** (length of longest axis/length of intermediate axis)	**Sphericity** ($36\pi \times Volume^2 / Surface\ Area^3$)	**Equivalent Spherical Radius (μm)** (radius of a sphere which has the same volume as the nucleus)	**Surface Area (μm^2)**	**Aspect Ratio** (Major Axis / Minor Axis)	**Circularity** ($4\pi \times Area / Perimeter^2$)	**Perimeter/ Circumference (μm)**
CPD n=56	1165±380	1.368±0.301	1.214±0.165	0.121±0.048	6±1	1176±530	1.132±0.185	0.725±0.091	51±9
EPC2 n=37	577±181	1.233±0.152	1.257±0.205	0.122±0.043	5±1	715±266	1.222±0.240	0.739±0.112	41±5

(a)

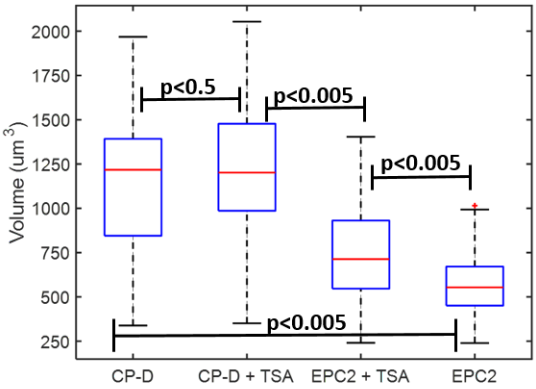

(b)

Figure 4.8: **(a)** Nuclear characteristics quantified for both the CP-D and EPC2 cell lines using 3D confocal imaging. **(b)** The mean volume and spread of the nuclear volume distribution for CP-D with and without TS-A as well as EPC2 with and without TS-A.

Several nuclear characteristics were quantified for both the CP-D and EPC2 cell lines using 3-D confocal imaging as shown in **Figure 4.8**. The most notable differences between the two cell lines can be found between the volume and surface area of the cells. The mean volume and spread of the nuclear volume distribution for CP-D with and without TS-A as well as EPC2 with and without TS-A in shown in **Figure 4.8**. All data is normally distributed and an ANOVA test determined that there is a significant difference between the 4 populations ($p=9.32x10^{-21}$). Further

Mann-Whitney testing has determined there is no statistically significant difference between the CP-D and CP-D with TS-A (p=0.4068). However there is a statistically significant difference between the EPC2 and EPC2 with TS-A (p=0.0024), between the CP-D and EPC2 ($p=1.9834x10^{-11}$), and between the CP-D with TS-A and the EPC2 with TS-A ($p=4.9258x10^{-9}$). TS-A is a histone deacetylase inhibitor and alters gene expression/epigenetic activity and has been shown to reduce the stiffness of the nucleus by decondensing the chromatin structure and making it more homogeneous. More condensed chromatin is associate with cancerous cells. This result tells us that TS-A is not effective in decondensing the chromatin in the CP-D cell line. The nuclear volume determined in this dissertation differs significantly from the results found by Nandakumar et al. [123], who state that the nuclear volume for EPC2 is 163±51 μm^3 and 432±188 μm^3 for CP-D. However, their study could have been compromised by the use of hematoxylin to stain the cells, as hematoxylin stains all nucleic acid whereas DAPI more selectively stains DNA. Additionally, the cells in the Nandakumar study were grown in a gel and imaged via 3-D tomography resulting in differences between our 2-D adhered cells and the 3-D cells in the Nandakumar study.

	Intensity RHF (Total Chromocenter Intensity / Nuclear Intensity)	**Volume RHF** (total chromocenter volume / nuclear volume)	**Total Number of Chromocenters**	**Mean Volume of Chromocenter(s) Per Nucleus (µm³)**	**Total Volume of Chromocenter(s) Per Nucleus (µm³)**	**Distance Border to Border Mean** (distance between chromocenter border to nuclear periphery)	**Distance Bary Center to Border Mean** (distance between chromocenter barycenter to nuclear periphery)
CPD n=58	0.026±0.009	0.017±0.015	37±16	0.495±0.205	16.698±5.514	0.567±0.194	1.206±0.260
EPC2 n=37	0.027±0.011	0.017±0.008	29±15	0.402±0.138	9.962±3.751	0.511±0.210	1.152±0.270

Table 4.2: Chromocenter characteristics quantified for both the CP-D and EPC2 cell lines using 3D confocal imaging.

Additionally, as shown in **Table 4.2** several chromocenter characteristics were also

quantified for both the CP-D and EPC2 cell lines using 3D confocal imaging. The most notable differences can be found between the total volume of the chromocenters per nucleus of the cells. Although intensity cannot be quantified, this result points to the idea that the CP-D chromatin is more heterogeneous in its distribution when compared to the EPC2 chromatin.

Finally, the number of nucleoli, the nucleoli volume, and the nuclear speckle volume were analyzed as shown in **Figure 4.9** and **Table 4.3**.

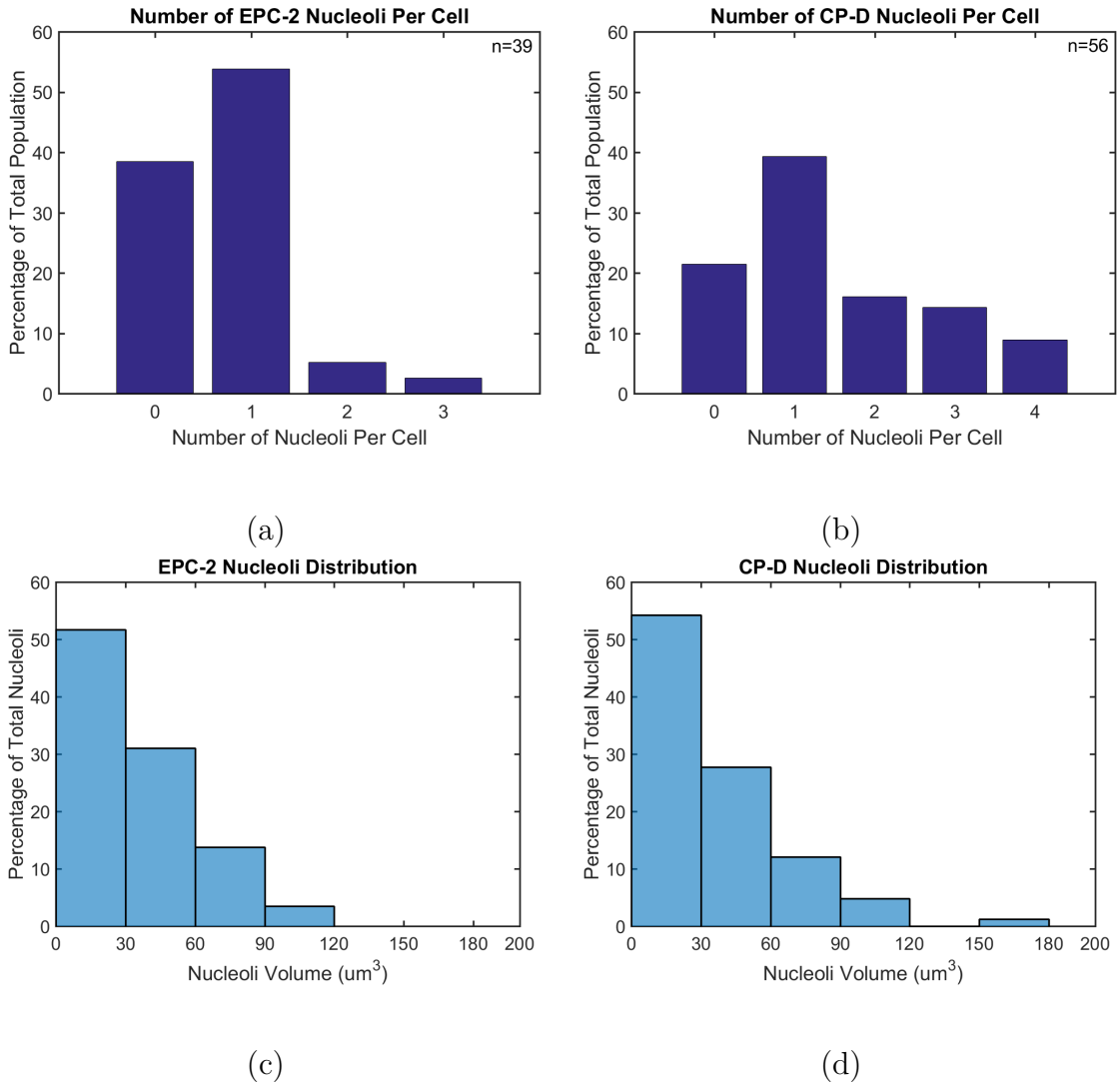

Figure 4.9: The number of nucleoli per cell in the EPC2 **(a)** and CP-D cell line **(b)**. The volume distribution of the nucleoli was also quantified for both the EPC2 **(c)** and CP-D cell lines **(d)**.

	Nuclear Speckle Volume (μm^3)	Nucleoli Volume (μm^3)	Volume of Nucleus (μm^3)	Nuclear Speckle Percentage	Nucleoli Volume Percentage
CPD n=56	117±116	48±37	1165±380	10.04%	4.12%
EPC2 n=39	34±25	27±29	577±181	5.89%	4.68%

Table 4.3: The nucleoli volume for each cell line as well as the nuclear speckle volume compared to the total volume of the cell nucleus.

The average number of nucleoli per cell was greater for the CP-D cell line (1.5±1.2) compared to the average number of nucleoli in the EPC2 cell line (0.7±0.7). While the CP-D nucleoli are larger than the EPC2 nucleoli, the nucleoli of both cell lines take up roughly the same volume percentage inside the nucleus. Almost all cancer types display large and/or increased number of nucleoli in the literature and can be used as a parameter for worsening prognosis [2, 3, 4, 5] so the CP-D result presented here is in good agreement with existing publications. The speckled regions of the nucleus represent the regions of large RNA concentration/mRNA production [124]. CP-D nuclear speckles occupy twice as much volume of the cell nucleus when compared to EPC2 nuclear speckles. This is an interesting result because it demonstrates that the mRNA production seems to be upregulated in cancer cells.

Conclusion and Future Work

We were able to detect the location of the missing DNA fraction which was previously undetected by Marilyn Sanders and quantify the amount of DNA in 2 different cell lines. Roughly 30-40 % of the total DNA in each cell line is released from the nucleus in the supernatant fraction and this is where most of the differences between each cell line's chromatin can be observed. CP-D shows a wider variation of DNA quantity in

each fraction when compared to EPC2. Both cell lines display differences in nuclear volume and surface area as well as the number and volume of chromocenters found in each cell. The CP-D cell line has a nuclear volume that is almost twice the size of the EPC2 which is in line with the fact that the CP-D contains about two times the chromatin found in the EPC2 as the EPC2 is a normal diploid line whereas the CP-D is a tetraploid line. Additionally, it seems the CP-D has more heterogenity in its chromatin distribution since the volume of the chromocenters is larger than that of the EPC2. The average number of nucleoli per cell was greater for the CP-D cell line (1.5 ± 1.2) compared to the average number of nucleoli in the EPC2 cell line (0.7 ± 0.7). While the CP-D nucleoli are larger than the EPC2 nucleoli, the nucleoli of both cell lines take up roughly the same volume percentage inside the nucleus. Almost all cancer types display large and/or increased number of nucleoli in the literature so the CP-D result presented here is in good agreement with existing publications. CP-D nuclear speckles occupy twice as much volume of the cell nucleus when compared to EPC2 nuclear speckles. This is an interesting result because it demonstrates that the mRNA production seems to be upregulated in cancer cells. Finally, the majority of the chromatin images taken with AFM show single nucleosomes. However, a portion of AFM images of the supernatant fractions of EPC2 reveal ring-like nucleosome structures and individual nucleosomes in the EPC2. At 4 mins, 8 min and 16 min, the chromatin exists as a combination of rings of nucleosomes ranging from 0.43-0.83 um in diameter depending on the Mnase digestion time and individual nucleosomes (details shown in **Figure 4.10**). For the CP-D cell line, at 2 mins, the chromatin is digested into single nucleosomes. At 4 mins, 8 min and 16 min, the chromatin exists as a combination of single nucleosomes and nucleosome clumps. No ring structures are observed in the CP-D chromatin.

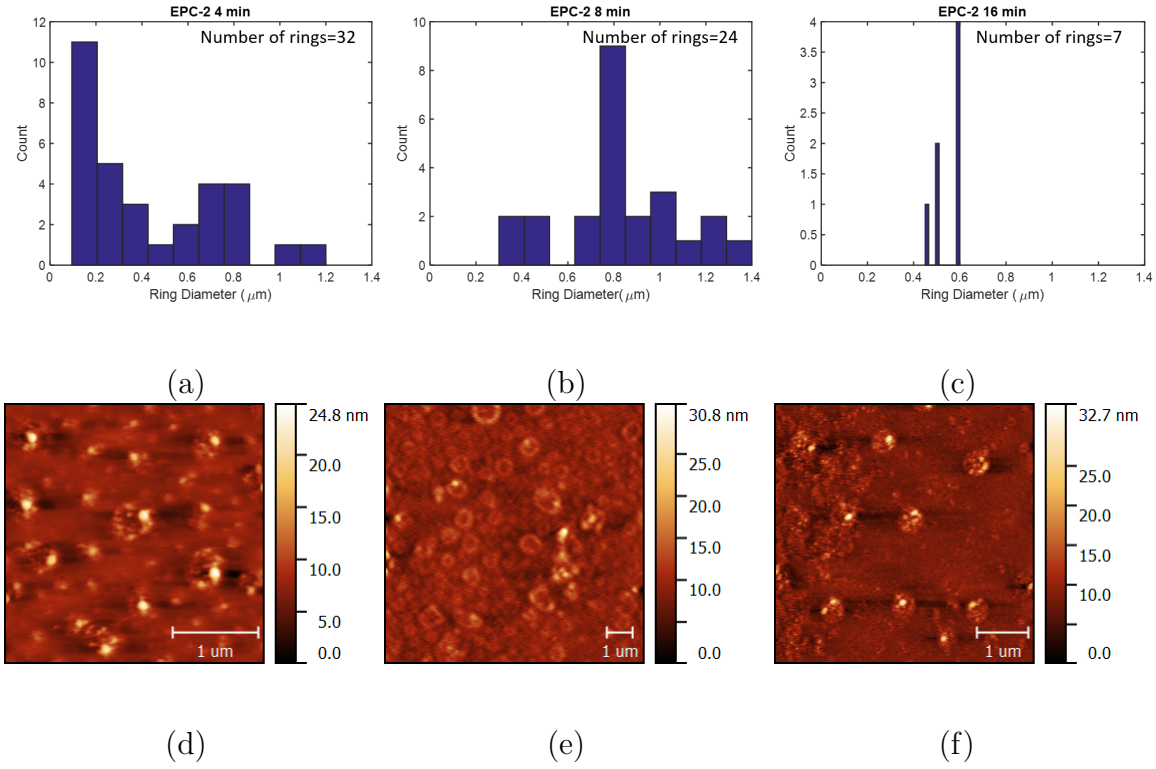

Figure 4.10: The mean diameter of the ring structures found in the EPC2 cell line at various Mnase digestion times.

As seen in **Figure 4.10**, The 8 min EPC2 fraction had a mean diameter size (0.831±0.255 μm) that was almost double that of the 4 min (0.438±0.306 μm) and 16 min fractions (0.550±0.065 μm). Additionally, the number of ring structures seems to decrease as Mnase digestion time gets longer, demonstrating that the Mnase slowly over time is able to digest these ring structures into single nucleosomes. It is believed that the bright circles in each ring are the protein cohesin. In the future, the mean nucleosome number (ring diameter) will be compared to DNA sequencing data to see if the two correlate in some manner. Additionally, more work will be done to identify the protein components of the ring structures.

Chapter 5

Quantifying the Stiffness Variation in Cancer Stem Cells and Non-Cancer Stem Cells Using AFM

This chapter details experiments that seek to determine if there is a correlation between breast CSCs and stiffness by combining confocal microscopy with AFM to directly correlate CD44/CD24 fluorescence levels with stiffness at the single cell level. It is hypothesized that since CSCs have been shown to correlate with the mesenchymal phenotype and follow some of the same pathways as the epithelial-to-mesenchymal transition that the CSCs would be softer than non-CSCs. Additionally, this experiment seeks to determine (1) if different buffer/environment conditions (PBS vs. HBSS) affect the stiffness of the different subpopulations (2) if it is possible to distinguish differences between the cellular cortex and intracellular network of CSCs and non-CSCs and (3) if there is a difference in the Young's Modulus of CSC and non-CSC nuclei. All experiments in this chapter were conducted by Nethmi Ariyasinghe.

5.1 Introduction

A recent concept that characterizes cancer cells is the cancer stem cell (CSC) concept. Al-Hajj et. al. discovered that only a minority of breast cancer cells have the ability to create new metastasis and isolated this sub-population of tumor-initiating cells based on cell surface markers [39]. These tumor-initiating cells (now called "cancer stem cells" in the field) possessed the CD44+/CD24- cell surface marker phenotype [39]. Cancer stem cells derive their name from the fact that, like traditional stem cells in the body, they possess the ability to self-renew and differentiate, the ability to persist in the body for long periods of time, and the ability to produce heterogeneous progeny [30]. The CSC concept treats tumor cells as a diverse population where only certain cells (the CSC cells) have the ability to proliferate extensively and potentially form new tumors [30]. In addition, the CD44+/CD24- phenotype is clinically associated with a poor prognosis for breast cancer patients making it even more necessary to determine what role CSC phenotypes play in cell mechanics [125]. It has been reported that changes in the cell stiffness (Young's Modulus) can affect the manner in which cells spread [126, 127]. In addition, it has been shown that the cell stiffness of metastatic cancer cells is softer than that of benign cells [59, 58, 121]. Furthermore, it has been shown that the stiffness of mature cells and stem cells differ [128]. Based on this information, we hypothesized that there should be a difference in the cell stiffness of stem-like cancer cells when compared to nonstem-like cancer cells. This chapter describes experiments designed to test if there is a correlation between breast CSCs and stiffness by (1) determining what percentage of the total population of cells are cancer stem-like cells in 3 different breast cancer cell lines (MDA-MB-231 (metastatic), MCF-7 (luminal), and MCF-10A (normal)) and (2) combining confocal with AFM to directly correlate CD44/CD24 levels with stiffness at the single cell level. CSCs have been shown to correlate with the mesenchymal phenotype and follow some of the same pathways as the epithelial-to-mesenchymal transition

[129, 130, 131, 60]. We would assume that since mesenchymal cells are softer than other cell types [132, 133, 134, 54], that the CSCs would be softer than the non-CSCs. Additionally, this experiment seeks to determine (1) if different buffer/environment conditions (PBS vs. HBSS) affect the stiffness of the different subpopulations of these cells since it has already been hypothesized that different buffer/environment conditions affect the percentage of each subpopulation of cells [135] (2) if there is a difference in the stiffness of stem-like cells when probed with a large/dull tip and a sharp tip (sharper tips allow deeper probing into the sample and provide a more localized analysis of the sample whereas larger tips aim to provide more of an average stiffness across the cell) and (3) if there is a difference in the Young's Modulus of the stem-like cell nuclei when compared to the non-stem-like cell nuclei.

5.2 Materials and Methods

5.2.1 AFM Experiments

5.2.2 Cell Culture

MDA-MB-231 cells were cultured in growth media prepared by creating a solution of 1x Dubecco's Modified Eagle Medium (DMEM) (Gibco # 11965092) with 10% fetal bovine serum (ATCC) by volume. MCF-10A cells were cultured in growth media prepared by mixing 500 ml of DMEM/F12 (Invitrogen #11330032) with 25 ml of horse serum (Invitrogen #16050122), 100ul of epidermal growth factor (EGF,100ug/ml stock solution, Gibco #PHG0311), 250ul of hydrocortisone (1mg/ml stock solution, Sigma #H0888), 50 μl of cholera toxin (1 mg/ml stock solution, Sigma #C8052), 500 μl of bovine insulin (10 mg/ml stock solution, Sigma #I1882), and 5 ml of penicillin/streptomycin (Invitrogen #15070063). MCF-7 cells were cultured in growth media prepared by mixing 56 ml of fetal bovine serum with 0.6 ml of bovine insulin

(10mg/ml stock solution) and 500 ml of Eagle's Minimum Essential Medium (EMEM) (ATCC). All growth media solutions were filtered before being stored at $-20°C$ for future use.

5.2.3 Sample Preparation

To create samples, cells were grown from ATCC cell lines in flasks with growth media for 3-4 days until cells reached 70% confluence (incubator conditions: 37°C and 5% CO_2). After reaching 70% confluence, 7.5 ml of 1x Dulbecco's Phosphate Buffer Saline (DPBS) (Gibco #14190144) were added to the culture flask to rinse the cells. Then 2 ml of Cellstripper (Corning #25056CI) were added, and cells were placed into the incubator for 10 minutes. Afterwards, 3 ml of growth media were mixed with the cell stripper/cell mixture in the flask, and the entire solution was transferred to a test tube and centrifuged at 900 RPM for 5 minutes at 25°C to separate the cell pellet from the supernatant. The supernatant was removed, and the cells were resuspended in 5 ml of growth media. Sample dishes were created by combining 1 ml of resuspended cells with 1 ml of growth media in a glass bottom 50 mm petri dish (World Precision Instruments). Samples were incubated at 37°C and 5% CO_2 for 24-48 hours before being analyzed. Initially, the remaining growth media in the petri dish was removed. Then 3 ml of blocking buffer (1% Bovine Serum Albumen (BSA) in phosphate buffered saline (PBS)) was added to the dish and incubated at 37°C for 30 minutes to minimize non-specific adsorption of the antibodies. In the meantime, CD44 (BD Pharmingen #560977) and CD24 (BD Pharmingen #561644) antibody solutions were diluted in blocking buffer (10μl antibody to 1 ml blocking buffer). Afterwards, the blocking buffer was removed from the petri dish, and 2 ml of each of the diluted antibody solutions were added. Samples were then incubated for one hour at 37°C. Finally, samples were washed three times in 1x PBS with each wash lasting for 5 minutes.

5.2.4 Fluorescence-Activated-Cell-Sorting

Fluorescence-activated-cell-sorting (FACS) (BD FACSAria IIu Cell Sorter) was used to sort MDA-MB-231 cells into stem-like and non-stem-like populations. The sorted cells were then plated for about 10 hours and analyzed for differences in cell stiffness between the two populations using AFM.

5.2.5 Confocal Microscopy

Measurements were conducted using a MicroTime 200 (PicoQuant, Germany) confocal laser scanning fluorescence microscope where scans were preformed in the XY direction to create an image 256x256 pixels wide. Scans were bidirectional with an acceleration of 20%, and with 10 learning loops. For the duration of the scan, the intensity of each laser was held at 3.45-3.6 a.u. Initially, with the shutters closed, a cell was found using the eyepiece of the microscope and brought into focus. Then the shutter was opened to allow the blue laser (470 nm) to pass and the intensity of the laser was adjusted to 3.53 a.u. The image was scanned. Next the blue laser shutter was turned off and the red laser (640 nm) shutter was switched on to allow the red laser to pass and the intensity of the laser was adjusted to 3.53 a.u. The image was scanned and saved. This method allowed each cell to be imaged using both lasers so that the CD44 signal and the CD24 signal could be processed separately so that if the fluorescence signal overlapped channels it would not affect the measurements. Then the next cell was located in the eyepiece and the process was repeated. However, this time the images were taken with the lasers in reverse order (the red laser image first and then the blue laser image) to prevent photobleaching bias. This process was repeated in an alternating manner. Samples were only analyzed up to four hours after the last PBS wash to avoid imaging dead cells which usually detached themselves from the glass surface of the petri dish. Also, if the viewing field permitted, multiple cells that were growing nearby were imaged together to collect more data.

However, cells that were overlapping one another were not used in the analysis to ensure that the intensity signal being analyzed was actually from the single cell and not incorporating intensity from overlapping cells.

5.2.6 Combined AFM Indentation and CLSM on Cells

Atomic force microscopy (AFM) was combined with confocal microscopy to determine the stiffness (Young's Modulus) of the stem-like cells (CD44+/CD24-) and non-stem-like cells (CD44+/CD24+, CD44-/CD24+,CD44-/CD24-) to assess if there was a difference between the two subpopulations in three breast cancer/non-cancer cell lines: MDA-MB-231 (highly metastatic cancer),MCF-7 (cancer), and MCF-10A (normal) in both HBSS and PBS. Additionally, a sharp tip and a mesoscopic tip were used to determine if there were differences between the two subpopulations in two cancer cell lines: MDA-MB-231 and MCF-7. The AFM and confocal fluorescence measurements were performed on a combined system consisting of an MFP-3D-BIO (Asylum Research) AFM and a Picoquant Microtime 200 confocal laser scanning microscope [136, 137, 138]. LRCH-750 (Team Nanotec) silicon AFM probes (mesoscopic tip), with half-angle 19° determined from electron microscopy and radius as specified by the manufacturer, were used (apex radius: 780 nm; tip height: 15μm). The set point used for measurements was 0.25 V. All AFM data was collected in contact imaging mode. The spring constant of the tip was determined using the thermal energy dissipation method [71, 139]; values ranged from (90-177 pN/nm). Measurements were conducted using SymPhoTime 5.13 at room temperature. Scans were preformed in the XY direction to create an image 256x256 pixels wide. The image was scanned and, afterwards, a 4x4 force map of the cell was performed and saved. Then the next cell was located in the eyepiece and the process was repeated. However, this time the images were taken with the lasers in reverse order (the red laser image first and then the blue laser image) to prevent photobleaching bias. Samples were only analyzed

up to four hours after the last PBS or HBSS wash to avoid imaging dead cells which usually detached themselves from the glass surface of the petri dish. Since each force map produced sixteen curves with sixteen Young's moduli, the Young's moduli were averaged to determine the average Young's modulus per cell. In addition, the contact point for each force curve was selected manually as shown in **Figure B.1** (Appendix B) since there is no perfect algorithm for determining the contact point automatically.

5.2.7 Combined AFM Indentation and CLSM on Cell Nuclei

Atomic force microscopy (AFM) was combined with confocal microscopy to determine the stiffness (Young's Modulus) of the nuclei of stem-like cells (CD44+/CD24-) and non-stem-like cells (CD44+/CD24+, CD44-/CD24+,CD44-/CD24-) to assess if there was a difference between the two subpopulations in the breast cancer cell line MDA-MB-231 (highly metastatic cancer) at room temperature. CLSM was performed as mentioned in the previous section. Samples were only analyzed up to four hours after the last PBS or HBSS wash to avoid imaging dead cells which usually detached themselves from the glass surface of the petri dish. Samples were indented once with a force of 30nN using a SHOCON tip. The contact point for each force curve was selected manually as shown in **Figure B.1** (Appendix B).

5.2.8 Image Processing and Analysis

To determine the particular phenotype of the cell in each image, cells were individually "cut" from the larger image and the cell region's intensity data was extracted and analyzed via MatLab (see Appendix B). The intensity of each cell was normalized to the perimeter of the cell as described in Appendix B to create a list of intensities. Then a statistical analysis was conducted on the list to determine the mean and standard deviation of the counts for the unstained cells. Any stained cell with a mean intensity three standard deviations above this was considered "positive" and

values below this threshold were considered to be "negative". This was to ensure that only the cells with the highest expression of each cell marker (either CD44 or CD24) were being assigned a positive value for that marker. In this manner, every cell analyzed was assigned to one of four categories: CD44+/CD24+, CD44+/CD24-, CD44-/CD24+, and CD44-/CD24- (**Figure 5.3**).

5.3 Results and Discussion

Fluorescence-activated cell sorting (FACS) is a standard technique used to sort subpopulations of cells based on the presence or absence of certain physical characteristics. We sought to utilize this technique to separate the stem-like and non-stem-like cell subpopulations for the breast cancer cell lines studied. Cells were sorted with FACS and then plated and analyzed 10 hours afterward (to give the cells enough time to adhere to the surface of the petri dish) using AFM to characterize the cell stiffness (Young's Modulus) of the subpopulations. However, we determined that there was no statistically significant difference between the cancer stem cell (CSC) and non-cancer stem cell populations (**Figure 5.1**). Measurements from 41 non-stem-like cells were compared to measurements of 50 stem-like (CD44+/CD24-) cells. The CSC pheonotype cells which are CD44+/CD24- have the same stiffness (mean stiffness: 0.50 $\pm$ 0.38 kPa) as their non-stem cell counterparts (mean stiffness: 0.51$\pm$ 0.38 kPa) when taking the standard deviation into account.

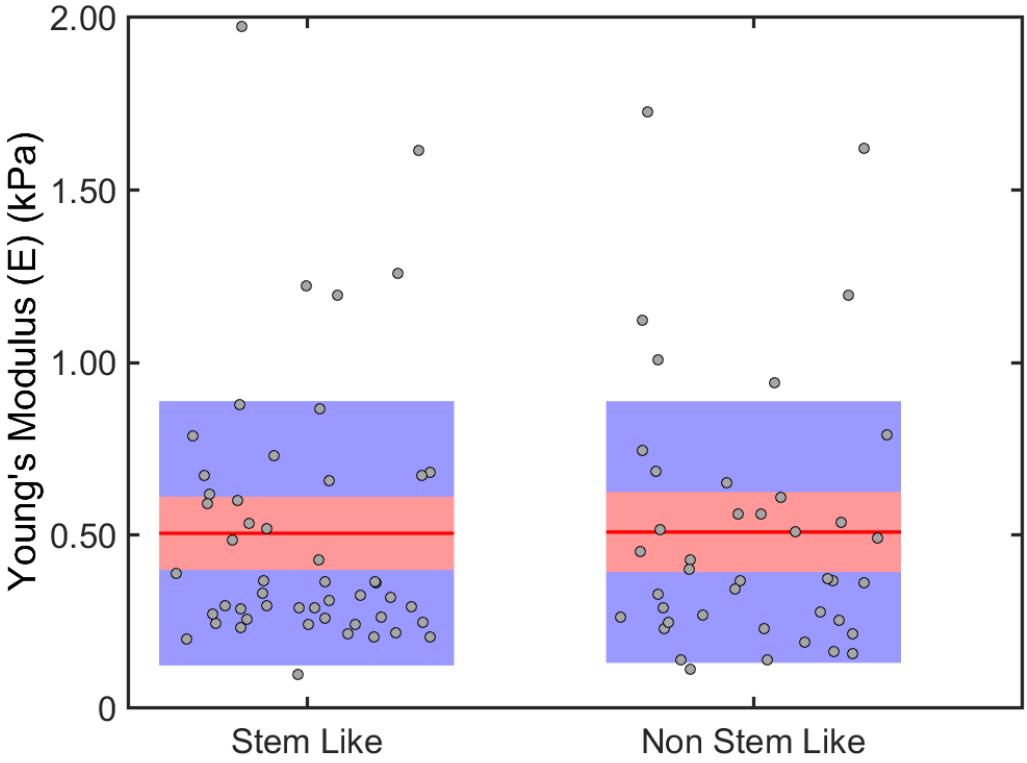

Figure 5.1: Stiffness of MDA-MB-231 Cell Subpopulations After FACS Sorting and Plating On Petri Dish.

CSC populations are commonly assessed with FACS; however, cell stiffness is altered by FACS either due to stress or due to waiting too long after plating cells (which may cause differentiation). Since the data shows that there was no statistically significant difference between stiffness for the CSC and non-CSC populations, it was determined that using FACS to sort CSCs and then measure their stiffness may not be the solution to eliminate other artifacts from affecting the cellular mechanics of our samples. We then grew the cells in a petri dish and fluorescently labeled the cells there so as not to disturb their growth. The stiffness of the non-stem-like and stem-like cells was determined using AFM and compared to the stiffness of the non-stem-like and stem-like cells sorted via FACS. These results are shown in **Figure**

5.2.

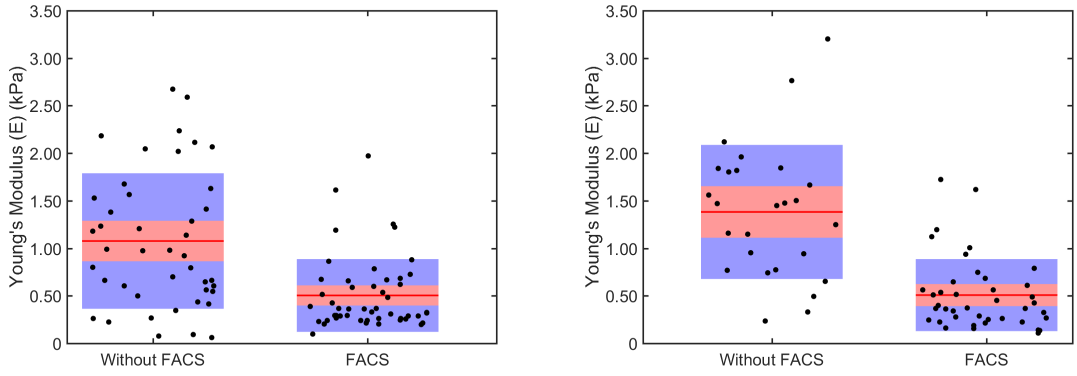

(a) (b)

Figure 5.2: **(a)** MDA-MB-231 stem-like cells were compared without FACS sorting (n=43) (mean stiffness:1.08 ± 0.71 kPa) and with FACS sorting (n=50) (mean stiffness: 0.50 ± 0.38 kPa). **(b)** MDA-MB-231 nonstem-like cells were compared without FACS sorting (n=26) (mean stiffness: 1.38 ± 0.71 kPa) and with FACS sorting (n=41) (mean stiffness: 0.51 ± 0.38 kPa).

For both stem-like and non-stem-like cells a Mann-Whitney test determined that there was a statistically significant difference between the FACS and non-FACS cell population (stem-like: p=1.7400x10^{-5}; non-stem-like: p=2.7454x10^{-7}). Thus, we decided to proceed with staining the cells while they were adhered to the surface of the petri dish instead of in solution as is required for FACS.

5.3.1 Characterization of Breast CSC Populations

Since all population characterization in the literature at this point had only been performed using FACS, we sought to determine the subpopulations of the stem-like and non-stem-like cells using confocal imaging as described in the Materials and Methods section for three breast cell lines: MDA-MB-231, MCF-7 and MCF-10A. The results of this population characterization is shown in **Figure 5.3** and **Table**

5.1. Samples were imaged in PBS buffer solution for up to 4 hours after antibody staining. All "positive" samples are three standard deviations above the mean for unstained; all others were labeled "negative" samples.

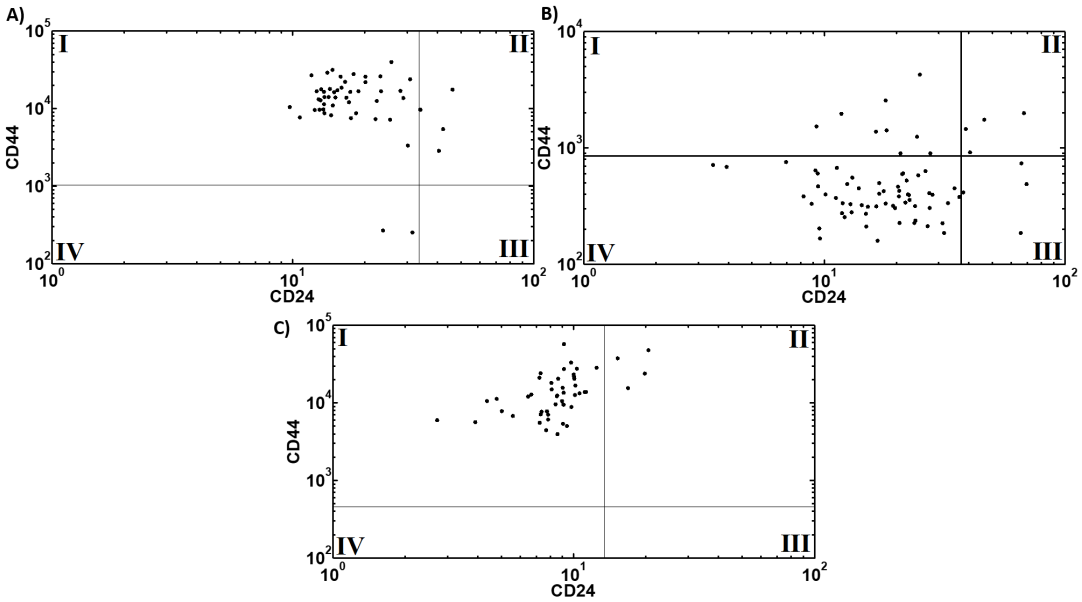

Figure 5.3: Log-Log Plots of CD44 and CD24 showing the subpopulations breakdown of each cell line: **A)** MDA-MB-231 **B)** MCF-7 **C)** MCF-10A in PBS buffer. Quadrant 1 shows all the CD44+/CD24- cells, Quadrant 2 is CD44+/CD24+, Quadrant 3 shows all the CD44-/CD24+, and Quadrant 4 is all the CD44-/CD24-.

A.

		Percentage of Total Population (%)			
Cell Line	**Buffer**	**CD44+/CD24+**	**CD44-/CD24+**	**CD44+/CD24-**	**CD44-/CD24-**
MDA-MB-231	PBS	8	0	87	4
	HBSS	3	0	76	21
MCF-7	PBS	5	5	12	77
	HBSS	0	0	21	79
MCF-10A	PBS	8	0	92	0
	HBSS	86	0	14	0

B.

		Percentage of Total Population (%)			
Cell Line	**Buffer**	**CD44+**	**CD44-**	**CD24+**	**CD24-**
MDA-MB-231	PBS	95	4	8	91
	HBSS	79	21	3	97
MCF-7	PBS	17	83	11	89
	HBSS	21	79	0	100
MCF-10A	PBS	8	92	100	0
	HBSS	100	0	86	14

Table 5.1: Subpopulations of cancer stem cells (CSCs) for MDA-MB-231 (n=51), MCF-7 (n=75), and MCF-10A (n=50) breast cancer cell lines determined using confocal microscopy **(A)** Subpopulations of both markers **(B)** Subpopulations of individual markers

In agreement with the literature, the MDA-MB-231 cell line has a majority of stem-like cells (87%) [140]. Unlike the majority of the literature, the MCF-7 cell line contains between 12-23% stem-like cells instead of $\geq$80% stem-like cells [135, 141]. However, this result is more similar to Tanaka et. al [142], who found 35% of MCF-7 cells were stem-like. Similarly, the MCF-10A cell line contains 92% stem-like cells whereas the literature reports only around 20% stem-like cells [135]. Differences between the results determined here and other publications indicate that different cell growth conditions might contribute to the differences in cell subpopulations as suggested by Sheridan et. al [135].

5.3.2 CSC Populations and Stiffnesses for Multiple Cell Lines Characterized By Multiple Tip Shapes and By Multiple Buffers

After identifying the individual subpopulations within each cell line, we then proceeded to determine the stiffness of the stem-like and non-stem-like populations within each of the three cell lines. These results are shown in **Figure 5.4**. As described earlier, it was difficult to find CSCs for the MCF-10A cell line in HBSS as this is a non-tumorogenic cell line. Mann-Whitney testing was used to determine statistical significance of differences between populations. Average stiffness for each cell was compiled by taking a 4x4 force map using a maximum force of 1 nN.

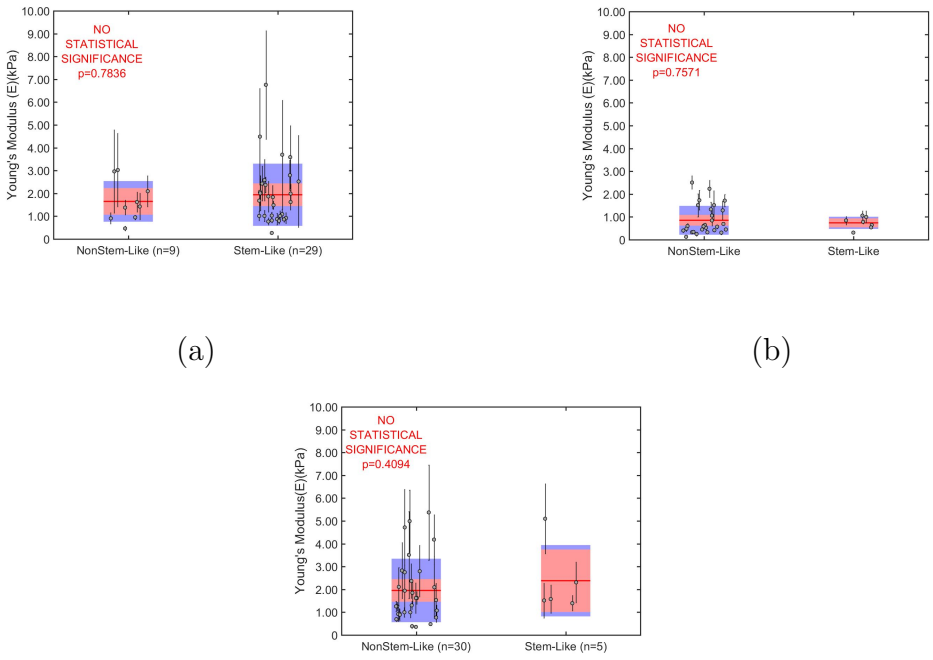

Figure 5.4: Boxplots showing the Young's Modulus of **(a)** MDA-MB-231 **(b)** MCF-7 and **(c)** MCF-10A cell subpopulations in HBSS.

As shown in **Figure 5.4a**, there is no significant stiffness difference between the

cancer stem cell (CSC) pheonotype cells (CD44+/CD24-) (mean stiffness of 1.94 ± 1.36 kPa) and the non-stem cell counterparts (mean stiffness of 1.65 ± 0.89 kPa) for the MDA-MB-231 cell line. Similarly, measurements from 7 stem-like cells (mean stiffness of 0.74 ± 0.27 kPa) showed no significant stiffness difference when compared to measurements from 28 non-stem-like cells (mean stiffness of 0.74 ± 0.27 kPa) for the MCF-7 cell line (**Figure 5.4b**). The same conclusion was true for cancer stem cell (CSC) pheonotype cells (mean stiffness of 2.38 ± 1.56 kPa) and the non-stem cell counterparts (mean stiffness of 1.95 ± 1.39 kPa) in the MCF-10A cell line (**Figure 5.4c**). However, there is a statistically significant difference between the three stem-like populations as determined by an ANOVA test (p=0.04992715). There is also a statistically significant difference between the three non-stem-like populations (p=0.01888). The MCF-10A stem-like cells and non-stem-like cells are stiffer than either the MDA-MB-231 or the MCF-7 which is in agreement with literature that states that normal cells are stiffer than cancerous cells. However, it is interesting to note that the MCF-7 are softer than the MDA-MB-231 cells which are a more malignant, mesenchymal cell line; this result could stem from the issue that only a small population of MCF-7 stem-like cells (n=7) and a small population of MDA-MB-231 non-stem-like cells (n=9) were able to be measured.

Next we compared the effect of two different buffer solutions (PBS and HBSS) and their impact on the stiffness of the stem-like cell populations. HBSS as a buffer induces cell starvation which promotes the enhancement of the Warburg effect and helps cells remain cancerous [143, 144, 145, 146]. Thus, we would expect the HBSS cells to be softer than the PBS cells.

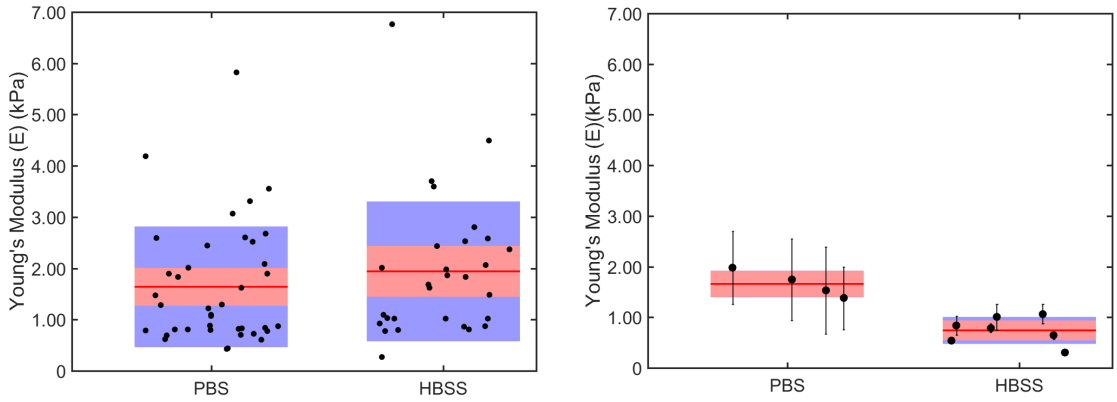

(a)

(b)

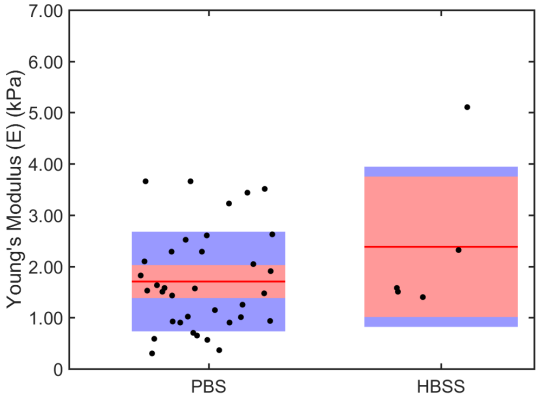

(c)

Figure 5.5: Stiffness of **(a)** MDA-MB-231 **(b)** MCF-7 and **(c)** MCF-10A stem-like cell subpopulations in PBS buffer and HBSS buffer.

As seen in **Figure 5.5a**, MCF-10A stiffness measurements from 35 cells in PBS (1.70 ± 0.97 kPa) were compared to measurements of 5 cells in HBSS (2.38 ± 1.56 kPa). A Mann-Whitney test has determined that there is no significant difference between the two populations (p=0.3263). Similarly, MCF-7 stiffness measurements from 4 cells in PBS (1.66 ± 0.26 kPa) were compared to measurements of 7 cells in HBSS (0.74 ± 0.27 kPa) (**Figure 5.5b**). A Mann-Whitney test has determined that there is a significant difference between the two populations (p=0.0061). Finally,

MDA-MB-231 stiffness measurements from 39 cells in PBS (1.64 ± 1.18 kPa) were compared to measurements of 29 cells in HBSS (1.94 ± 1.36 kPa) (**Figure 5.5c**). A Mann-Whitney test has determined that there is not a significant difference between the two populations (p=0.1887).

It is interesting to see that HBSS buffer has no statistically significant stiffness effect on MCF-10A stem-like cells. We would hypothesize that since this is a normal breast cell line, the HBSS would induce the Warburg effect on the stem-like cells making them more cancerous and therefore, softer than their PBS counterparts. This hypothesis may indeed still be true for a larger sample size; however, it is difficult to find stem-like cells in the MCF-10A population as it is a normal breast cell line and is not expected to contain stem-like cells.

Next we took the two cancer cell lines and compared the stiffness of stem-like and non-stem-like cells using a larger tip size to determine if there were any differences between the subpopulations of cells that could be probed on an intracellular level instead of the cortical level as was done with the sharp tip. Cells were measured for 4 hours after staining with CD44 and CD24 antibody. All cells were indented to a depth of 1.5μm.

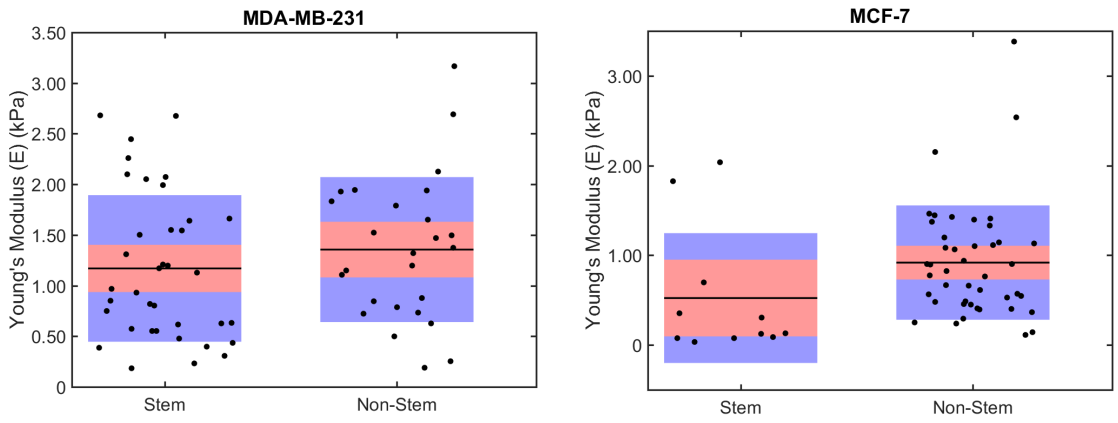

(a) (b)

Figure 5.6: Large tip indentation results. **(a)** Young's modulus of MDA-MB-231 cell subpopulations. Measurements from 26 non-stem-like cells (mean Young's modulus: 1.38 ± 0.71 kPa) were compared to measurements of 37 stem-like cells (mean Young's modulus:1.08 ± 0.71 kPa). **(b)** Young's modulus of MCF-7 cell subpopulations. Measurements from 43 non-stem-like cells (mean Young's modulus: 1.07± 0.66 kPa) were compared to measurements of 13 stem-like (CD44+/CD24-) cells (mean Young's modulus: 0.39±0.27 kPa).

The results of the large tip indentation analysis in **Figure 5.6** show that there is no statistically significant difference as determined by a Mann-Whitney test (p=0.08852) between the two populations for the MDA-MB-231 cell line. However, a Mann-Whitney test has determined that there is a statistically significant difference between the two populations for the MCF-7 ($p=3.8856 \times 10^{-5}$). These results are in accordance with our hypothesis that there would be no difference within the subpopulations of the MDA-MB-231 cell line as all the cells are mesenchymal and therefore are very malignant and cancerous. However, since the MCF-7 is a luminal cell line we would expect that the stem-like subpopulation would be softer than the non-stem-like cells since the stem-like population is observed to behave more like a mesenchymal cell line.

Next we compared the stiffness values between the large and the sharp tip for stem-like and non-stem-like populations for the MDA-MB-231 and the MCF-7 cell lines (**Figure 5.7**) to determine if any information could be gained from the cellular cortex and the intracellular network.

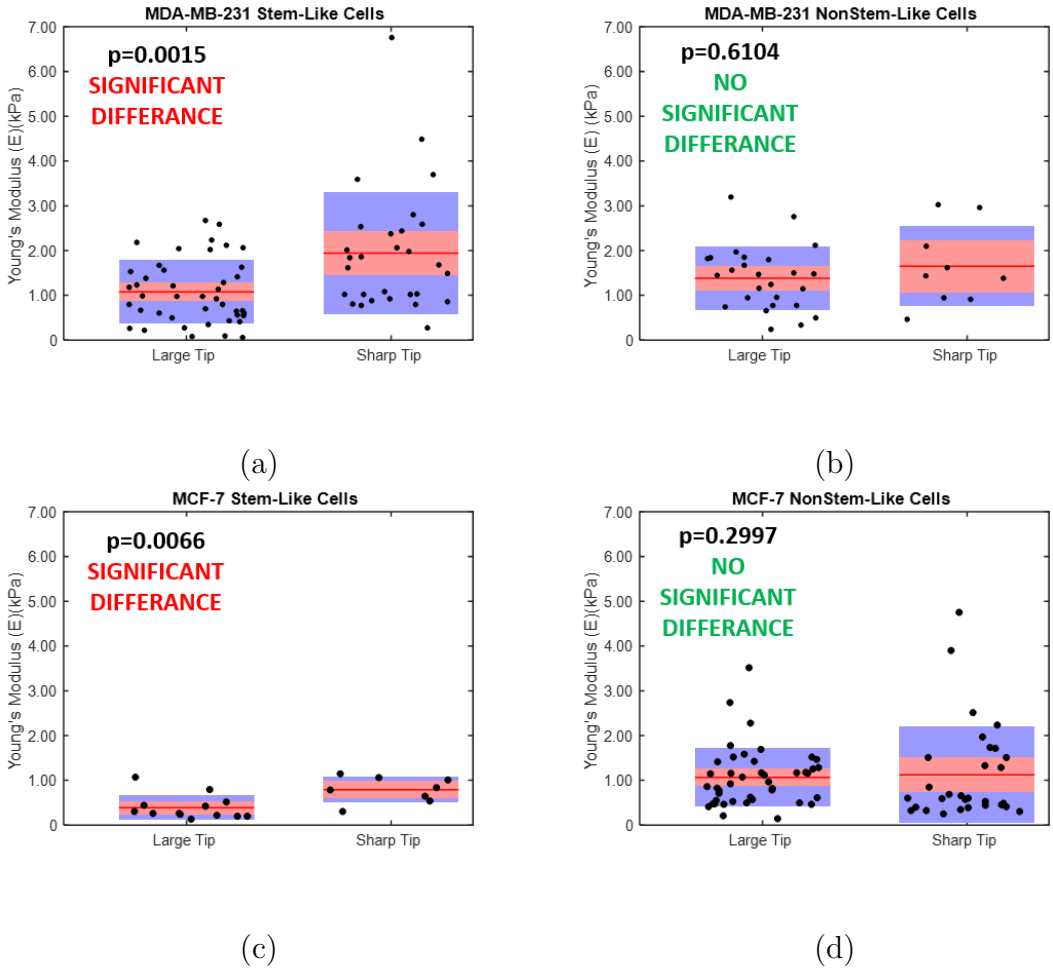

Figure 5.7: **(a)** Young's modulus of MDA-MB-231 stem-like cell subpopulations when analyzed with a larger tip (n=43) and a sharp tip (n=29). **(b)** Young's modulus of MDA-MB-231 non-stem-like cell subpopulations when analyzed with a larger tip (n=26) and a sharp tip (n=9). **(c)** Young's modulus of MCF-7 stem-like cell subpopulations when analyzed with a larger tip (n=13) and a sharp tip (n=8). **(d)** Young's modulus of MCF-7 non-stem-like cell subpopulations when analyzed with a larger tip (n=43)and a sharp tip (n=30).

Young's modulus of MDA-MB-231 stem-like cell subpopulations were analyzed with a larger tip (n=43) and a sharp tip (n=29) (**Figure 5.7a**). Mann-Whitney testing was used to determine whether or not there was a statistically significant difference between all populations. The cells probed with a large tip show a reduced stiffness (mean Young's modulus: 1.08 ± 0.71 kPa) than the cells probed with a sharp tip (1.94 ± 1.36 kPa). However, the Young's modulus of MDA-MB-231 non-stem-like cell subpopulations when analyzed with a larger tip (n=26) (mean stiffness: 1.38 ± 0.71 kPa) and a sharp tip (n=9) (mean stiffness: 1.65 ± 0.89 kPa) show no significant stiffness difference between the two populations (**Figure 5.7b**). Similarly, the Young's modulus of MCF-7 stem-like cell subpopulations when analyzed with a larger tip (n=13) and a sharp tip (n=8) (**Figure 5.7c**) show that the cells probed with a large tip are less stiff (mean Young's modulus: 0.39± 0.71 kPa) than the cells probed with a sharp tip (mean Young's modulus: 0.79 ± 0.29 kPa) whereas the stiffness of MCF-7 non-stem-like cell subpopulations when analyzed with a larger tip (n=43) (mean stiffness: 1.07± 0.5 kPa) and a sharp tip (n=30) (mean stiffness:1.12 ± 1.08 kPa) showed no statistically significant difference between the two populations (**Figure 5.7d**). Large tip probes can give us information about the intracellular network whereas the sharp tip can give us information about the cellular cortex. Based on this, it appears that there are differences between the cellular cortex and the intracellular network of the stem-like subpopulations whereas differences between these two areas of the cells either are not significant enough to be determined for the non-stem-like populations or these differences do not exist.

5.3.3 Cancer Stem Cell Nuclei

Finally, a super sharp silicon tip (radius of curvature=6 nm, pyramidal; k=0.3N/m) was used to probe stiffness differences between stem-like and non-stem-like nuclei of MDA-MB-231 cells (**Figure 5.8**).

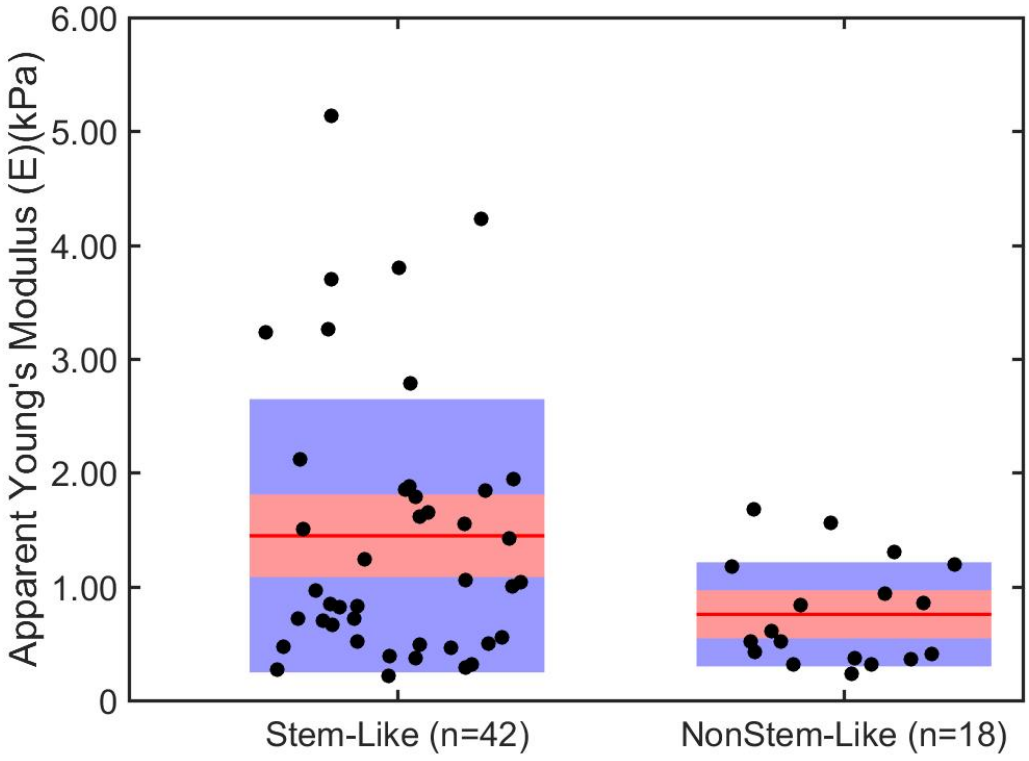

Figure 5.8: Apparent Young's Modulus of MDA-MB-231 nuclei for cell subpopulations. Measurements from 18 non-stem-like cells were compared to measurements of 42 stem-like (CD44+/CD24-) cells.

Each cell nuclei was indented only once with a force of 30 nN and analyzed from a depth of 0.25-2.5 μm. The cancer stem cell (CSC) phenotype nuclei are more stiff (mean Young's Modulus: 1.45± 1.20 kPa) than their non-stem-like nuclei counterparts (mean Young's Modulus: 0.76 ± 0.46 kPa). A Mann-Whitney test has determined that there is a statistically significant difference between the two populations (p=0.0288).

5.4 Conclusion

5.4.1 Cancer Stem Cell Population Characterization via Confocal

The MDA-MB-231 cell line possesses the most CSCs in its population (87%) compared to the MCF-10A cell line, which possesses no CSCs in its population, and the MCF-7 cell line, which possesses 12% CSCs. The subpopulation results obtained from confocal microscopy agree well with Sheridan et. al.'s results for the MDA-MB-231 cells [135]. However, the results for the CD24 marker for both Sheridan et. al. and the confocal imaging both sharply disagree with the findings from Lu et.al. [135, 141]. The MCF-10A results are quite a bit different from Sheridan et.al.; however, this can be attributed to the difference in cell growth conditions which Sheridan et. al. believe to play a large role in determining the phenotype of MCF-10A cells [135]. The MCF-7 results also differ from the populations found in the literature for yet undetermined reasons [135, 141, 147, 148, 149, 150, 151, 142]. The differences between groups could be due to the smaller sampling size of the confocal microscopy technique compared to the other groups' FACS (fluorescence-activated cell sorting) sample size or the growth conditions of the cells when cultured. One hypothesis would be that growth conditions deeply impact the generation of cancer stem cell phenotypes since all four groups use different cell culture growth conditions. The impact of cell growth conditions on subpopulations of CSCs would be interesting to study in a future work as this has been alluded to in the literature but never properly studied [135].

5.4.2 Buffer Impact on Stiffness and CSC Subpopulation

There seem to be no statistically significant differences in the stiffness when comparing between the stem-like and nonstem-like populations of each cell line in HBSS (**Figure 5.4**) when using the sharp tip. However, there is a statistically significant

difference when the stem-like populations between the 3 cell lines are compared in HBSS (**Figure 5.4**). A statistically significant difference existed for the nonstem-like populations between the 3 cell lines in HBSS (**Figure 5.4**) as well. Additionally, there is a statistically significant difference between stem-like cells grown in PBS buffer versus HBSS buffer for the MCF-7 cell line proving that the buffer environment does in fact affect the stiffness of cell subpopulations for some cell lines (**Figure 5.5**). The MCF-7 is impacted by buffer environment whereas the MDA-MB-231 and the MCF-10A cell lines are not. MCF-7 cells are stiffer when measured in PBS buffer compared to HBSS buffer (**Figure 5.5**).

5.4.3 Impact of Tip Size on Stiffness and CSC Subpopulation

There is a significant stiffness difference between stem cells and non-stem cells in the MCF-7 cell line which does not occur in the MDA-MB-231 cell line for the larger tip (**Figure 5.6**). These differences could be attributed to differences in cell phenotype for the cell lines. MDA-MB-231 cells are mesenchymal so it agrees with our hypothesis that there is no difference between CSCs and non-CSCs cell stiffness; on the other hand the MCF-7 cell line is luminal so the CSCs being more mesenchymal-like would be softer than the non-CSCs. Additionally, there is a significant stiffness difference between stem cells probed with the large tip when compared to the stem cells probed with the sharp tip for both the MDA-MB-231 cell line and the MCF-7 cell line. The same is not true for the non-stem-like cells for both cell lines (**Figure 5.7**). This could signify that there are differences between the cell body and cell cortex for the stem-like cells for both cell lines but not for the non-stem-like cells for both cell lines since the sharper tip is more sensitive to the cell cortex whereas the large tip is more sensitive to the cell body [152].

5.4.4 Nuclei Stiffness Between CSCs and Non-CSCs

There is a statistically significant difference between the nuclei of stem-like and non-stem-like MDA cells as hypothesized. Since more metastatic cancer cell lines have softer nuclei [68, 153], we anticipated that the nuclei of the stem-like cells would be softer than their non-stem-like counterparts. However, the results show the opposite. Softer nuclei have been shown to have decreased chromatin condensation and low lamin A/C levels [153] so it is possible that our results demonstrate that the non-stem-like cells have a decreased chromatin condensation and low lamin A/C levels.

Chapter 6

Conclusion and Future Work

This dissertation has presented novel physical science-based methods to quantify qualitative characteristics of biological organisms. Chapter 4 introduced a method to quantify DNA in several cancer/non-cancer cell lines as well as methods to quantify nuclear size, chromocenters, nucleoli size and quantity per cell as well as nuclear speckle regions of the cellular nucleus between cancer and non-cancer cells. Chapter 5 detailed methods and applications of combined atomic force microscopy and CLSM to determine the Young's Modulus between stem-like and non-stem-like cells in cancer and non-cancer breast cell lines.

While methods discussed here are in relation to cancer, the quantitative methodology can be applied to many different types of cells and tissues to study the effects of disease and pathogens. Chapter 4 presents methods to quantify DNA extracted from cells as well as quantitative methods to study nuclear size, chromatin distribution, nucleoli size and nuclear speckle distribution in mammalian cells. Finally the novel discovery of ring structures in the EPC2 normal esophageal cell line compared to the CP-D cancerous esophageal cell line leaves the possibility open for future studies to determine the size of these structures and whether they are held together by cohesin and/or condensin.

Chapter 5 presents new methods to study cell phenotype and how it alters cell mechanics. It was determined that the MCF-7 stem-like cells are impacted by buffer environment whereas the MDA-MB-231 and the MCF-10A cell lines are not. MCF-7 cells are stiffer when measured in PBS buffer compared to HBSS buffer due to the Warberg effect. Additionally, there is a significant stiffness difference between stem cells and non-stem cells in the MCF-7 cell line which does not occur in the MDA-MB-231 cell line for the larger tip. These differences could be attributed to differences in cell phenotype for the cell lines. MDA-MB-231 cells are mesenchymal so it agrees with our hypothesis that there is no difference between CSCs and non-CSCs cell stiffness; on the other hand the MCF-7 cell line is luminal so the CSCs being more mesenchymal-like would be softer than the non-CSCs. Finally, there is a statistically significant difference between the nuclei of stem-like and non-stem-like MDA cells as hypothesized. Since more metastatic cancer cell lines have softer nuclei [68, 153], it was anticipated that the nuclei of the stem-like cells would be softer than their non-stem-like counterparts. However, the results show the opposite to be true and raise the possibility for further investigation. Softer nuclei have been shown to have decreased chromatin condensation and low lamin A/C levels [153] so it is possible that the results presented here demonstrate that the non-stem-like cells have a decreased chromatin condensation and low lamin A/C levels.

Lord Kelvin is attributed to have said: "When you can measure what you are speaking about, and express it in numbers, you know something about it." Biological organisms, due to their complexity and heterogeneity, have typically been characterized only qualitatively due to the lack of techniques to quantify what has been qualitatively observed. In this dissertation, qualitative biology has been quantitatively analyzed in the hopes of gaining further insight into the mechanics of cancer biology.

Bibliography

[1] Siegel RL, Miller KD, Jemal A. Cancer statistics, 2018. *CA Cancer J Clin.*, 2018.

[2] MacCarty WC. The value of the macronucleus in the cancer problem. *Am. J. Cancer*, 26:529–532, 1936.

[3] Derenzini M, Montanaro L, and Trere D. What the nucleolus says to a tumour pathologist. *Histopathology*, 54(6):753–62, 2009.

[4] Derenzini DM, Betts CM, Ceccarelli C, and Eusebi V. Ultrastructural organization of nucleoli in benign nevi and malignant melanomas. *Virchows Arch. B-Cell Pathol. Incl. Mol. Pathol.*, 52(4):343–52, 1986.

[5] Derenzini M, Nardi F, Farabegoli F, Ottinetti A, Roncaroli F, and Bussolati G. Distribution of silver-stained interphase nucleolar organizer regions as a parameter to distinguish neoplastic from nonneoplastic reactive cells in human effusions. *Acta Cytol.*, 33(4):491–8, 1989.

[6] Watson JD and Crick FH. Molecular structure of nucleic acids. *Nature*, 1953.

[7] Struhl K and Segal E. Determinants of nucleosome positioning. *Nat Struct Mol Biol*, 20:267273, 2013.

[8] Mavrich TN, Ioshikhes IP, Venters BJ, Jiang C,Tomsho LP, Qi J, Schuster SC, Albert I & Pugh BF. A barrier nucleosome model for statisticalpositioning of nucleosomes throughout the yeast genome. *Genome Res*, 18(7):1073–83, 2008.

[9] Travers A and Muskhelishvili G. DNA structure and function. *FEBS*, 282(12):2279–2295, 2015.

[10] Felsenfeld G and Groudine. Controlling the double helix. *Nature*, 421(6921):448–53, 2003.

[11] Felsenfeld G. Chromatin. *Nature*, 271:115122, 1978.

[12] Ramakrishnan V. Histone Structure and the organization of the nucleosome. *Annual Rev Biophys Biomol Struct.*, 26:83–112, 1997.

[13] Marino-Ramirez L, Kann MG, Shoemaker BA, Landsman D. Histone structure and nucleosome stability. *Expert Rev. Proteomics*, 2:719–729, 2005.

[14] Baldwin JB, Boseley PG, Bradbury EM, and Ibel K. The subunit structure of the eukaryotic chromosome. *Nature*, 253:245249, 1975.

[15] Gilbert N, Boyle S, Fiegler H, Woodfine K, Carter NP, and Bickmore WA. Chromatin Architecture of the Human Genome: Gene-Rich Domains Are Enriched in Open Chromatin Fibers. *Cell*, 118(5):555–66, 2004.

[16] Grewal SI and Jia S. Heterochromatin revisted. *Nat. Rev. Genet.*, 8:3546, 2007.

[17] Shukla V, Vaissiere T, and Herceg Z. Histone acetylation and chromatin signature in stem cell identity and cancer. *Mutation Research*, 637(1-2):1–15, 2008.

[18] Dillon,N. Heterochromatin Structure and Function. *Biol Cell*, 96(8):631–637, 2004.

[19] Gilbert N and Allan J. Distinctive Higher-Order Chromatin Structure at Mammalian Centromeres. *Proc Natl Acad Sci U S A*, 98(21):1194911954, 2001.

[20] Thoma F, Koller T, and Klug A. Involvement of Histone H1 in the Organization of the Nucleosome and of the Salt-Dependent Superstructures of Chromatin. *J Cell Biol*, 83(2.1):403–27, 1979.

[21] Woodcock CL, Frado LL, and Rattner JB. The Higher-Order Structure of Chromatin: Evidence for a Helical Ribbon Arrangement. *J Cell Biol*, 99(1.1):42–52, 1984.

[22] Song F, Chen P, Sun D, Wang M, Dong L, Liang D, Xu RM, Zhu P, and Li G. Cryo-Em Study of the Chromatin Fiber Reveals a Double Helix Twisted by Tetranucleosomal Units. *Science*, 344(6182):376–80, 2014.

[23] Eltsov M, Maclellan KM, Maeshima K, Frangakis AS, and Dubochet J. Analysis of Cryo-Electron Microscopy Images Does Not Support the Existence of 30-Nm Chromatin Fibers in Mitotic Chromosomes in Situ. *Proc Natl Acad Sci U S A*, 105(50):19732–7, 2008.

[24] Belmont AS and Bruce K. Visualization of G1 Chromosomes: A Folded, Twisted, Supercoiled Chromonema Model of Interphase Chromatid Structure. *J Cell Biol*, 127(2):287–302, 1994.

[25] Zhou Z and Irudayaraj J. A Native Chromatin Extraction Method Based on Salicylic Acid Coated Magnetic Nanoparticles and Characterization of Chromatin. *Analyst*, 140(3):938–44, 2015.

[26] Behjati. Distinct H3F3A and H3F3B driver variants define chondroblastoma and giant cell tumour of bone. *Nat Genet.*, 45(12):14791482, 2013.

[27] Encyclopdia Britannica. Cutaway drawing of a eukaryotic cell. *https://www.britannica.com/science/eukaryote/images-videos/media/195150/112877*, April 2019.

[28] Raven P,Johnson G,Mason K, Losos J, and Singer S. Biology 11th edition. *McGraw Hill*, 2017.

[29] Bapat S. *Cancer Stem Cells: Identification and Targets*. Wiley, 2008.

[30] Tannishtha Reya, Sean J. Morrison, Michael F. Clarke, and Irving L. Weissman. Stem cells, cancer and cancer stem cells. *Nature*, 414(6859):105–11, 2001.

[31] Bao S, Wu Q, McLendon RE, Hao Y, Shi Q, Hjelmeland AB, Dewhirst MW, Bigner DD, and Rich JN. Glioma stem cells promote radioresistance by preferential activation of the DNA damage response. *Nature*, 444:4756760, 2006.

[32] Diehn M, Cho RW, Lobo NA, Kalisky T, Dorie MJ, Kulp AN, Qian D, Lam, JS, Ailles LE, Wong M. Association of reactive oxygen species levels and radioresistance in cancer stem cells. *Nature*, 458:780783, 2009.

[33] Ishikawa F, Yoshida S, Saito Y, Hijikata A, Kitamura H, Tanaka S, Nakamura R, Tanaka T, Tomiyama H, Saito N. Chemotherapy-resistant human AML stem cells home to and engraft within the bone-marrow endosteal region. *Nat. Biotechnol.*, 25:13151321, 2007.

[34] Saito Y, Uchida N, Tanaka S, Suzuki N, Tomizawa-Murasawa M, Sone A, Najima Y, Takagi S, Aoki Y, Wake A. Induction of cell cycle entry eliminates human leukemia stem cells in a mouse model of AML. *Nat. Biotechnol.*, 28:1275280, 2010.

[35] Viale A, De Franco F, Orleth A, Cambiaghi V, Giuliani V, Bossi D, Ronchini C, Ronzoni S, Muradore I, Monestiroli S. Cell-cycle restriction limits DNA damage and maintains self-renewal of leukaemia stem cells. *Nature*, 457:5156, 2009.

[36] Zhang M, Atkinson RL, and Rosen JM. Selective targeting of radiation-resistant tumor-initiating cells. *Proc. Natl. Acad. Sci.*, 107:35223527, 2010.

[37] Kreso A, Dick JE. Evolution of the cancer stem cell model. *Cell Stem Cell*, 14(3):275–91, 2014.

[38] Bonnet D, Dick JE. Human acute myeloid leukemia is organized as a hierarchy that originates from a primitive hematopoietic cell. *Nat. Med.*, 3(7):730–7, 1997.

[39] Al-Hajj M, Wicha MS, Benito-Hernandez A, Morrison SJ, Clarke MF. Prospective identification of tumorigenic breast cancer cells. *Proceedings of the National Academy of Sciences USA*, 100(7):3983–8, 2003.

[40] Kelly PN, Dakic A, Adams JM,et. al. Tumor growth need not be driven by rare cancer stem cells. *Science*, 317(5836):337, 2007.

[41] Hill RP and Perris R. "Destemming" cancer stem cells. *J Natl Cancer Inst*, 99(19):1435–40, 2007.

[42] Velasco-Velzquez MA, Homsi N, De La Fuente M, Pestell RG. Breast Cancer Stem Cells. *Int J Biochem Cell Biol.*, 44(4):573–7, 2012.

[43] McCulloch EA. Stem cells in normal and leukemic hemopoiesis. *Blood*, 62(1):1–13, 1983.

[44] Baumann P, Cremers N, Kroese F, Orend G, Chiquet-Ehrismann R, Uede T, et al. CD24 expression causes the acquisition of multiple cellular properties associated with tumor growth and metastasis. *Cancer Res.*, 65(23):10783–93, 2005.

[45] Blick T, Widodo E, Hugo H, Waltham M, Lenburg ME, Neve RM, et al. Epithelial mesenchymal transition traits in human breast cancer cell lines. *Clin Exp Metastasis*, 25(6):629–42, 2008.

[46] Goodison S, Urquidi V, Tarin D. CD44 cell adhesion molecules. *Journal of Clinical Pathology:Moecular Pathology*, 52(4):189–196, 1999.

[47] Bourguignon LY, Zhu H, Chu A, et al. Interaction between the adhesion receptor, CD44, and the oncogene product, p185HER2, promotes human ovarian tumor cell activation. *J Biol Chem*, 272(44):27913–8, 1997.

[48] Birch M, Mitchell S, Hart IR. Isolation and characterization of human melanoma cell variants expressing high and low levels of CD44. *Cancer Res*, 51(24):6660–7, 1991.

[49] Sy MS, Guo YJ, Stamenkovic I. Distinct effects of two CD44 isoforms on tumor growth in vivo. *J Exp Med*, 174(4):859, 1991.

[50] Brunner TB, Kunz-Schughart LA, Grosse-Gehling P, Baumann M. Cancer stem cells as a predictive factor in radiotherapy. *Semin Radiat Oncol.*, 22(2):151–74, 2012.

[51] Fang X, Zheng P, Tang J, and Liu Y. CD24: from A to Z. *Cellular and Molecular Immunology*, 7(2):100–103, 2010.

[52] Park SY, Lee HE, Li H, et.al. Heterogeneity for stem-cell related markers according to tumor subtype and histologic stage in breast cancer. *Clinal Cancer Research*, 16(3):876–87, 2010.

[53] Lekka MP. Laidler D, Gil J, Lekki Z, Stachura A, and Hrynkiewicz Z. Elasticity of normal and cancerous human bladder cells studied by scanning force microscopy. *European Biophysics Journal*, 28(4):312316, 1999.

[54] Li QS, Lee GY , Ong CN and Lim CT. AFM indentation study of breast cancer cells. *Biochem. Biophys. Res. Commun.*, 374:609–613, 2008.

[55] Nikkhah M, Strobl J. MCF10A and MDA-MB-231 human breast basal epithelial cell co-culture in silicon micro-arrays. *Biomaterials*, 32(30):7625–32, 2011.

[56] Butcher DT, Alliston T, and Weaver VM. A tense situation: forcing tumour progression. *Nature Rev. Cancer*, 9(2):108–22, 2009.

[57] Sinkus R. High-resolution tensor MR elastography for breast tumour detection. *Phys. Med. Biol.*, 45(6):1649–64, 2000.

[58] Plodinec M, Loparic M, Monnier C, Obermann E, Zanetti-Dallenbach R,Oertle P, Hyotyla J, Aebi U, Bentires-Alj M, Lim R and Schoenenberger C. The nanomechanical signature of breast cancer. *Nature Nanotechnology*, 7:757765, 2012.

[59] Cross SE, Jin YS, Rao J, Gimzewski JK. Nanomechanical analysis of cells from cancer patients. *Nature Nanotechnology*, 2(12):708–703, 2007.

[60] Kotiya S and Bhattacharya S. Breast cancer stem cells, EMT and therapeutic targets. *Biochemical and Biophysical Research Communications*, 453:112–116, 2014.

[61] Fawcett, DW. *An Atlas of fine structure(The Cell).* W.B Saunders Company, 1966.

[62] Denais C and Lammerding J. Nuclear Mechanics in Cancer. *Advanced Experimental Medical Biology*, 773:435–470, 2014.

[63] Zink D, Fischer AH, Nickerson JA. Nuclear Structure in Cancer Cells. *Nat Rev Cancer*, 4(9):677–87, 2004.

[64] Ho CY and Lammerding J. Lamins at a glance. *J Cell Sci*, 125(9):2087–2093, 2012.

[65] de Las Heras JI, Batrakou DG, Schirmer EC. Cancer biology and the nuclear envelope: a convoluted relationship. *Semin Cancer Biol*, 23(2):125–37, 2013.

[66] Lammerding J, Schulze PC, Takahashi T, Kozlov S, Sullivan T, Kamm RD, Stewart CL, Lee RT. Lamin A/C deficiency causes defective nuclear mechanics and mechanotransduction. *J Clin Invest*, 113(3):6370378, 2004.

[67] Swift J,Ivanovska IL, Buxboim A, Harada T, Dingal PCDP, Pinter J, Pajerowski JD, Spinler KR, Shin JW, Tewari M. Nuclear Lamin-A Scales with Tissue Stiffness and Enhances Matrix-Directed Differentiation. *Science*, 341(6149):1240104, 2013.

[68] Liu H, Wen J, Xiao Y, Liu J, Hopyan S, Radisic M, Simmons CA, and Sun Y. In Situ Mechanical Characterization of the Cell Nucleus by Atomic Force Microscopy. *ACS Nano*, 8(4):38213828, 2014.

[69] Gerber C. Binnig G, Quate CF. Atomic force microscope. *Phys. Rev. Lett.*, 56:930–933, Mar 1986.

[70] Doss B. Quantifying Mechanical Heterogeneity in 3D Biological Systems with the Atomic Force Microscope. *Arizona State University, PhD dissertation*, 2015.

[71] Hutter JL and Bechhoefer J. Calibration of atomic-force microscope tips. *Rev. Sci. Instrum.*, 7:1868–1873, 1993.

[72] Cook SM. Practical implementation of dynamic methods for measuring atomic force microscope cantilever spring constants. *Nanotechnology*, 17(9), 2006.

[73] Kasas S, Longo G, and Dietler G. Mechanical Properties of biological specimans explored by atomic force microscopy. *Journal of Physics D: Applied Physics*, 46(13):133001, 2013.

[74] Radmacher M. Studying the mechanics of cellular processes by atomic force microscopy. *Methods Cell Biol.*, 83:347–72, 2007.

[75] Lin DC and Horkay F. Nanomechanics of polymer gels and biological tissues: A critical review of analytical approaches in the Hertzian regime and beyond. *Soft Matter*, 4(4), 2008.

[76] Sneddon IN. The Relationship Between Load and Penetration in the Axisymmetric Boussinesq Problem for a Punch of Arbitrary Profile. *International Journal of Engineering Science*, 3(1):47–57, 1965.

[77] Hertz H. Uber die Beruhrung fester elastischer Korper. *Journal fr die reine und angewandte Mathematik*, 92, 1882.

[78] Staunton JR, Doss BL, Ros R. Correlating confocal microscopy and atomic force indentation reveals metastatic cancer cells stiffen during invasion into collagen I matrices. *Scientific Reports*, 2016.

[79] Frantz C, Stewart KM, and Weaver VM. The extracellular matrix at a glance. *J. Cell. Sci.*, 123(24):4195–4200, 2010.

[80] Discher DE, Mooney DJ, and Zandstra PW. Growth factors, matrices, and forces combine and control stem cells. *Science*, 324(5935):1673–7, 2009.

[81] Trappmann B and Chen CS. How cells sense extracellular matrix stiffness: A material's perspective. *Current Opinion Biotechnology*, 24(5):948–53, 2013.

[82] Garcia JR and Garcia AJ. Cellular mechanotransduction: Sensing rigidity. *Nature Materials*, 13(6):539–40, 2014.

[83] Lv H. Mechanism of regulation of stem cell differentiation by matrix siffness. *Stem Cell Res. Therapy*, 6(1):103, 2015.

[84] Engler AJ, Sen S, Sweeney HL, and Discher DE. Matrix elasticity directs stem cell lineage specification. *Cell*, 126(4):677–89, 2006.

[85] Hu S. Multiparametric bomechanical and biochemical phenotypic profiling of single cancer cells using an elasticity microcytometer. *Small*, 12(17):2300–11, 2016.

[86] Remmerbach TW, Wottawah F, Dietrich J, Lincoln B. Oral cnacer diagnosis by mechanical phenotyping. *Cancer Research*, 69(5):1728–32, 2009.

[87] Rodriguez ML, McGarry PJ, Sniadecki NJ. Review on cell mechanics:Experimental and modeling approaches. *Appl.Mech.Rev.*, 65(6):060801, 2013.

[88] Moeendarbary E and Harris AR. Cell mechanics: Principles, practices, and prospects. *Syst. Biol. Med.*, 6(5):371–88, 2014.

[89] Kuznetsov YG, Malkin AJ, and McPherson A. Atomic Force Microscopy Studies of Living Cells: Visualization of Motility, Division, Aggregation, Transformation, and Apoptosis. *J. Struct. Biol.*, 120(2):180–91, 1997.

[90] Henderson E, Haydon PG, and Sakaguchi DS. Actin filament dynamics in living glial cells imaged by atomic force microscopy. *Science*, 257(5078):1944–6, 1992.

[91] Schneider SW, Sritharan SW, Geibel JP, Oberleithner H, and Jena B. Surface dynamics in living acinar cells imaged by atomic force microscopy: Identification of plasma membrane structures involved in exocytosis. *Proc. Natl. Acad. Sci*, 94(1):316–321, 1997.

[92] Suresh S. Biomechanics and biophysics of cancer cells. *Acta Mater.*, 55(12):413–438, 2007.

[93] Hou HW, Li Q, Lee G, Kumar A, Ong C, and Lim CT. Deformability study of breast cancer cells using microfluidics. *Biomed. Microdevices*, 11(3):557–64, 2009.

[94] Cavallaro U and Christofori G. Cell adhesion and signalling by cadherins and Ig-CAMs in cancer. *Nat. Rev. Cancer*, 4(2):118–32, 2004.

[95] Reinhart-King CA. Cancer Cell Mechanics. *Physical Sciences and Engineering Advances in Life Sciences and Oncology (Springer*, 2016.

[96] Rianna C and Radmacher M. Cell mechanics as a marker for diseases: Biomedical applications of AFM. *AIP Conference Proceedings*, 1760(1), 2016.

[97] Sanderson MJ, Smith I, Parker I, Bootman MD. Fluorescence Microscopy. *Cold Spring Harbor Protocols*, 10, 2014.

[98] Minsky M. Memoir on Inventing the Confocal Scanning Microscope. *Scanning*, 10, 1988.

[99] Fellers TJ and Davidson MW. Introduction to Confocal Microscopy. *Olympus Fluoview Resource Center. National High Magnetic Field Laboratory*, 2007.

[100] Jonkman J and Brown, CM. Any Way You Slice It–A Comparison of Confocal Microscopy Techniques. *Journal of Biomolecular Techniques*, 26(2):54–65, 2015.

[101] Pawley JB. Handbook of Biological Confocal Microscopy. 2006.

[102] Hyde AM , Zultanski SL, Waldman JH, Zhong Y, Shevlin M, and Peng F. General Principles and Strategies for Salting-Out Informed by the Hofmeister Series. *Org. Process Res. Dev.*, 21(9):13551370, 2017.

[103] Grover, PK, Ryall, RL. Critical Appraisal of Salting-Out and its Implications for Chemical and Biological sciences. *Chem. Rev.*, 105(1):1–10, 2005.

[104] Long FA and McDevit WF. Activity Coefficients of Nonelectrolyte Solutes in Aqueous Salt Solutions. *Chem. Rev.*, 51(1):119169, 1952.

[105] Breslow R. Hydrophobic Effects on Simple Organic Reactions in Water. *Acc. Chem. Res.*, 24(6):159164, 1991.

[106] Blokzijl W and Engberts JBFN. Hydrophobic Effects. Opinions and Facts. *Angew. Chem., Int. Ed. Engl.*, 32(11):545–1579, 1993.

[107] Mancera, RL. Does Salt Increase the Magnitude of the Hydrophobic Effect? A Computer Simulation Study. *Chem. Phys. Lett.*, 296(5-6):459–465, 1998.

[108] Sanders MM. Fractionation of nucleosomes by salt elution from micrococcal nuclease-digested nuclei. *Journal of Cell Biology*, 79(1):97–109, 1978.

[109] Ganguli I. The first commercial UV-vis spectrophotometer. *The Scientist*, 2006.

[110] Nilapwar SM,Nardelli M,Westerhoff HV, Verma M. Absorption Spectroscopy. *Methods in Enzymology*, 500(1):59–75, 2011.

[111] Mrabet Y. Single beam scanning spectrophotometer. 2008.

[112] Fully Automatic Double Beam - Atomic Absorption Spectrophotometer (AA 8000).

[113] Sambrook J and Russell D. Detection of DNA in Agarose Gels. *Cold Spring Harbor*, 2006, 2001.

[114] Glasel J. Validity of nucleic acid purities monitored by 260/280 absorbance ratios. *BioTechniques*, 18(1):62–3, 1995.

[115] CP-D (CP-18821) ATCC CRL-4030.

[116] Senapathy S. Studying Biomolecular Structure and Their Interaction Using Atomic Force Microscopy. *Arizona State University, PhD Dissertation*, 2015.

[117] Henikoff S, Henikoff JG, Sakai A, Loeb GB, and Ahmad K. Genome-wide profiling of salt fractions maps physical properties of chromatin. *Genome Res*, 19(3):460–9, 2009.

[118] Burton K. Determination of DNA concentration with diphenylamine. *Methods Enzymol*, 12(Part B):163–166, 1968.

[119] Dische Z. *Mikrochemie*, 8, 1930.

[120] Webb J and Levy H. A Sensitive Method for the Determination of Deoxyribonucleic Acid in Tissues and Microorganisms. *J.Biol. Chem.*, 1954.

[121] Fuhrmann A, Staunton JR, Nandakumar V, Banyai N, Davies PCW and Ros R. AFM stiffness nanotomography of normal, metaplastic and dysplastic human esophageal cells. *Physical Biology*, 8(1):1–18, 2011.

[122] Poulet A, Arganda-Carreras I, Legland D, Probst AV, Andrey P, Tatout C. NucleusJ: an ImageJ plugin for quantifying 3D images of interphase nuclei. *Bioinformatics*, 31(7):1144–6, 2015.

[123] Nandakumar V, Kelbauskas L, Johnson R, and Meldrum D. Quantitative characterization of preneoplastic progression using single-cell computed tomography and three-dimensional karyometry. *Cytometry A*, 79(1):25–34, 2011.

[124] Spector DL and Lamond AI. Nuclear Speckles. *Cold Spring Harbor Perspectives in Biology*, 3(2):a000646, 2010.

[125] Giatromanolaki A, Sivridis E, Fiska A, Koukourakis MI. The CD44+/CD24- phenotype relates to 'triple-negative' state and unfavorable prognosis in breast cancer patients. *Medical Oncology*, 28(3):745–52, 2011.

[126] Bhadriraju, K and Hansen LK. Extracellular matrix- and cytoskeleton-dependent changes in cell shape and stiffness. *Exp. Cell Res.*, 278(1):92–100, 2002.

[127] Discher D, Janmey P, and Wang Y. Tissue cells feel and respond to the stiffness of their substrate. *Science*, 310:1139–1143, 2005.

[128] Titushkin I and Cho M. Modulation of Cellular Mechanics during Osteogenic Differentiation of Human Mesenchymal Stem Cells. *Biophysical Journal*, 93(10):36933702, 2007.

[129] Findlay VJ,Wang C, Watson D, and Camp ER. Epithelial to mesenchymal transition and the cancer stem cell phenotype:Insights from cancer biology with therapeutic implocations for colorectal cancer. *Cancer Gene Therapy*, 21(5):181–187, 2014.

[130] Morel A,Lievre M, Thomas C, Hinkal G, Ansieau S, and Puisieux A. Generation of Breast Cancer Stem Cells through Epithelial-Mesenchymal Transition. *Plos One*, 3(8):e2888, 2008.

[131] Mallini P, Lennard T, Kirby J, and Meeson A. Epithelial-to-mesenchymal transition:what is the impact on breast cancer stem cells and drug resistance. *Cancer Treatment Reviews*, 40:341–348, 2014.

[132] Jonas O, Mierkea CT and Ks JA. Invasive cancer cell lines exhibit biomechanical properties that are distinct from their noninvasive counterparts. *Soft Matter*, 7(24):11488, 2011.

[133] Suresh S. Connections between single-cell biomechanics and human disease states: gastrointestinal cancer and malaria. *Acta Biomaterialia*, 1:15–30, 2005.

[134] Suresh S. Biomechanics and biophysics of cancer cells. *Acta Biomater.*, 3:413–438, 2007.

[135] Sheridan C, Kishimoto H, Fuchs R, Mehrotra S, Bhat-Nakshatri P, Turner C, Goulet Jr. R, Badve S, and Nakshatri H . CD44+/CD24- breast cancer cells exhibit enhanced invasive properties: an early step necessary for metastasis. *Breast Cancer Research*, 8(5):R59, 2006.

[136] Fuhrmann A, Staunton JR, Nandakumar V, Banyai N, Davies P, and Ros R. AFM stiffness nanotomography of normal, metaplastic and dysplastic human esophageal cells. *Physical Biology*, 8(1):015007, 2011.

[137] Schulz O, Koberling F, Walters D, Koenig M, Viani J, Ros R. Simultaneous single molecule atomic force and fluorescence lifetime imaging. *Proc. of SPIE*, 7571:757109, 2010.

[138] Schulz O, Zhao Z, Ward A, Koenig M, Koberling F, Liu Y, Enderlein J, Yan H, and Ros R. Tip induced fluorescence quenching for nanometer optical and topographical resolution. *Optical Nanoscopy*, 2(1):10.1186/2192–2853–2–1, 2013.

[139] Butt HJ and Jaschke M. Calculation of thermal noise in atomic force microscopy. *Nanotechnology*, 6:1–7, 1995.

[140] Ricardo S. Breast cancer stem cell markers CD44, CD24, and ALDH1: expression distribution within intrinsic molecular subtype . *Journal of Clinical Pathology*, 64(11):937–946, 2011.

[141] Lu S and Labhasetwar V. Drug resistant breast cancer cell line displays cancer stem cell phenotype and responds sensitively to epigenetic drug SAHA. *Drug Delivery Transl. Res.*, 3(2):183–194, 2003.

[142] Tanaka H, Nakamura M, Kameda C, Kubo M, Sato N, Kuroki S, Tanaka M, and Katano M. The Hedgehog Signaling Pathway Plays an Essential Role in Maintaining the CD44+CD24-/low Subpopulation and the Side Population of Breast Cancer Cells. *AntiCancer Research*, 29:2147–2157, 2009.

[143] Xu. *Experimental Immunology*, 2014.

[144] Wu C, Chao Y,Shiah S, and Lin W. Nutrient deprivation induces the Warburg effect through ROS/AMPK-dependent activation of pyruvate dehydrogenase kinase. *Biochimica et Biophysica Acta*, 1833:1147–56, 2013.

[145] Yoon S, Woo SU, Kang JH, Kim K, Kwon MH, Park S, Shin HJ, Gwak HS, and Chwae YJ. STAT3 transcriptional factor activated by reactive oxygen species induces IL6 in starvation-induced autophagy of cancer cells. *Autophagy*, 6(8):1125–38, 2010.

[146] Zou Z, Yuan Z, Zhang Q, Long Z, Chen J, Tang Z, Zhu Y, Chen S, Xu J, Yan M, Wang J, Liu Q. Aurora kinase A inhibition-induced autophagy triggers drug resistance in breast cancer cells. *Autophagy*, 8(12):1798–810, 2012.

[147] Sun H, Jia J, Wang X, Ma B,Di L, Song G, and Ren J. CD44+/CD24- breast cancer cells isolated fron MCF-7 cultures exhibit enhanced angiogenic properties. *Clin. Transl. Oncol.*, 15:4654, 2013.

[148] Huang M, Zhang F, and Zhang Y. Influence factors on the formation of mammospheres from breast cancer stem cells. *Journal of Peking University (Health Sciences)*, 40(5):500–504, 2008.

[149] Croker A, Goodale D, Chu J, Postenka C, Hedley B, Hess D, and Allan A. High aldehyde dehydrogenase and expression of cancer stem cell markers selects for breast cancer cells with enhanced malignant and metastatic ability. *Journal of cellular and molecular medicine*, 13(8b):2236–2252, 2009.

[150] Lu XQ, Suo Z, Ma CL, Xu KJ, Liu YS, and Li HX. Quantity and distribution of CD44+/CD24-cells in breast cancer tissue and the cell lines. *Zhonghua bing li xue za zhi Chinese journal of pathology*, 38(7):441–444, 2009.

[151] Gong C, Yao H, Liu Q, Chen J, Shi J, Su F, and Song E. Markers of tumor-initiating cells predict chemoresistance in breast cancer. *PloS one*, 5(12):e15630, 2010.

[152] Vahabikashi A, Park CY, Perkumas K, Zhang Z, Deurloo EK, Wu H, Weitz DA, Stamer WD, Goldman RD, Fredberg JJ, Johnson M. Probe Senstivity to Cortical vs. Intracellular Cytoskeletal Network Stiffness. *Biophysical Journal*, 116(3):518–529, 2019.

[153] Khan ZS, Santos JM, and Hussain F. Aggressive prostate cancer cell nuclei have reduced stiffness. *Biomicrofluidics*, 12(1):014102, 2018.

Appendix A

RKO DNA QUANTIFICATION RESULTS

DNA gel electrophoresis was done in 0.8% agarose gel after isolating the DNA from chromatin using a phenol chloroform and ethyl ether extraction. DNA was loaded in the gel after being mixed with a 6X DNA loading dye and run for 2 hours at 60 V using 1X TAE as the running buffer.

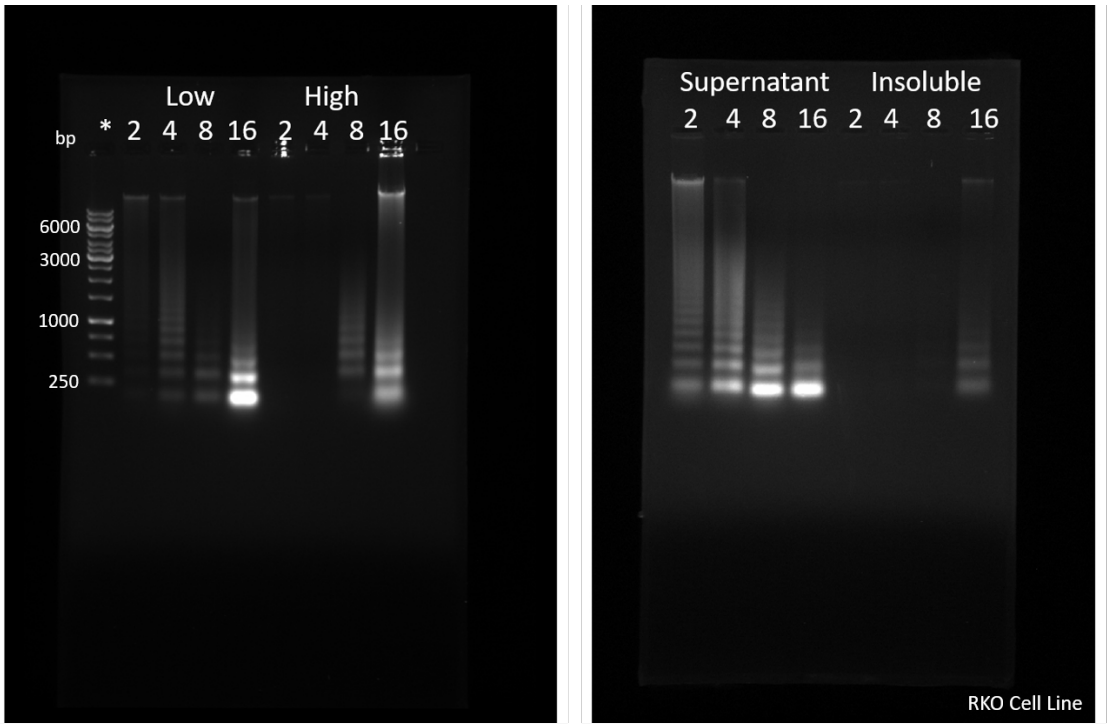

Figure A.1: Gel electrophoresis results for DNA extracted from the RKO cell line. The gel on the left shows the DNA contained in the low salt and high salt fractions at 2, 4, 8, and 16 minutes. The asterisk represents a DNA ladder used as a control. The gel on the right shows the DNA contained in the supernatant and insoluble fractions at 2, 4, 8 and 16 minutes.

Clearly, the gels in **Figure A.1** show that there is indeed DNA found in the supernatant fraction as well as the insoluble fraction at each digestion time proving that Sanders could have potentially discarded a portion of her DNA unintentionally. The figure below shows the total amount of DNA quantified for the RKO cell line.

Cell Line/Trial	DNA per cell (µg) ($x10^{-5}$)	Supernantant Fraction (µg)	Low Salt Fraction (µg)	High Salt Fraction (µg)	Insoluable Fraction (µg)	Total Quantity Extracted (µg)	Quantity of Cells Counted (millions)	Expected DNA Quantity (µg)	Percent Discrepancy (%)
RKO Trial 1	1.4	160	39	30	30	259	38	525	51
RKO Trial 2	1.4	165	84	44	25	318	38	525	39
RKO Trial 3	1.4	170	162	254	113	699	40.8	563	24

Table A.1: The total amount of DNA obtained from each salt fraction shown here along with the theoretical quantity of DNA expected based on the total number of cells for the RKO cell line.

Appendix B

CONTACT POINT SELECTION

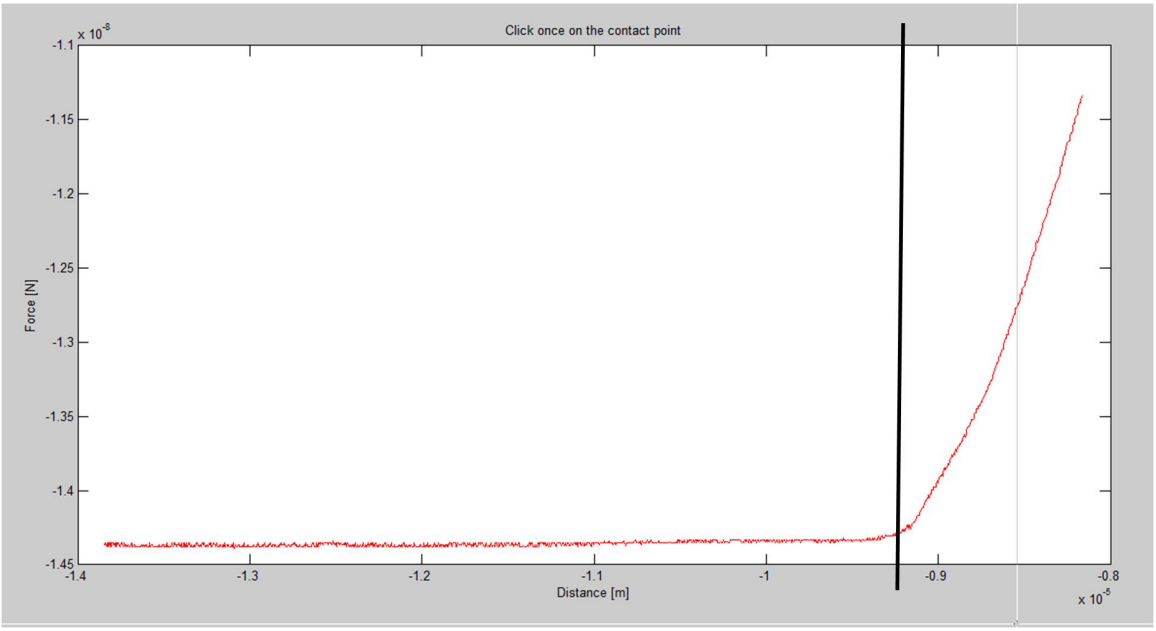

Figure B.1: An example of a force curve taken with the AFM. The black line represents the hypothetical location of a hand-selected contact point.

Appendix C

IMAGE PROCESSING AND ANALYSIS

To cut a cell from the larger image, the image was opened in SymPhoTime 5.13 and the "select free ROI" tool was selected. Then the mouse was used to trace around the cell and the cell's intensity data was saved (**Figure C.1**).

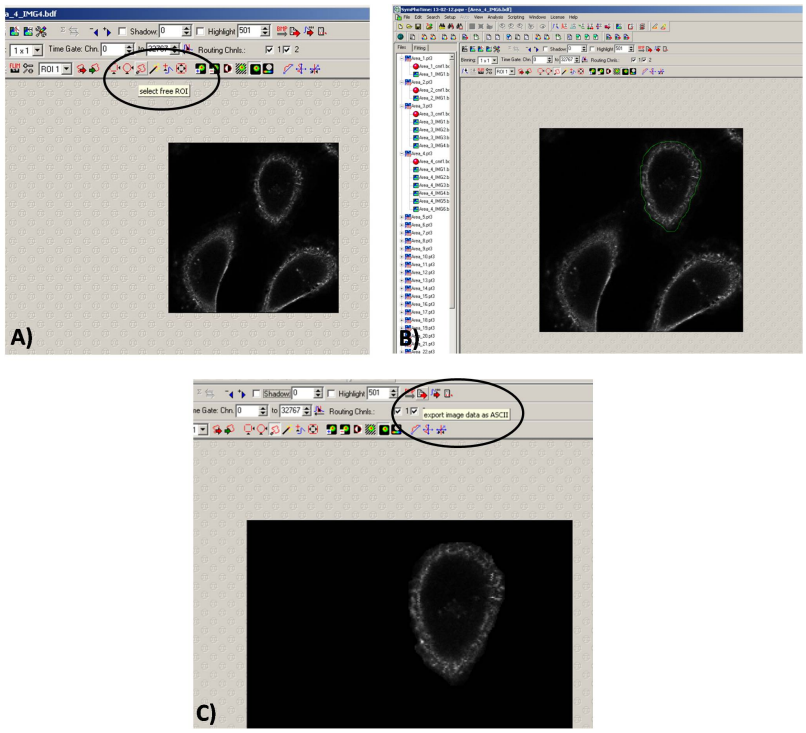

Figure C.1: Steps taken to cut cell intensity data from the larger image and import into analysis software. These images show a cell stained for CD44.

At times (most notably with the CD24 signal), it was hard to view the entire cell in the image (see **Figure C.2**).

To ensure that the same cell had the same area being cut, an overhead film was placed over the brighter cell image and the outline of the cell was traced using a Sharpie. Then the film was placed over the dimmer cell image and the "select free ROI" tool in SymPhoTime was used to cut out the exact same cell area as the brighter image by tracing over the Sharpie outline.

Once all the cells were cut, the intensity data was imported to MatLab. There the intensity of each cell was normalized to the perimeter of the cell (normalized perimeter value= total intensity of the cell/total perimeter of the cell) and the results were saved. Thresholds for whether a cell was positive or negative for a particular stem cell marker needed to be determined. Therefore unstained sample dishes were

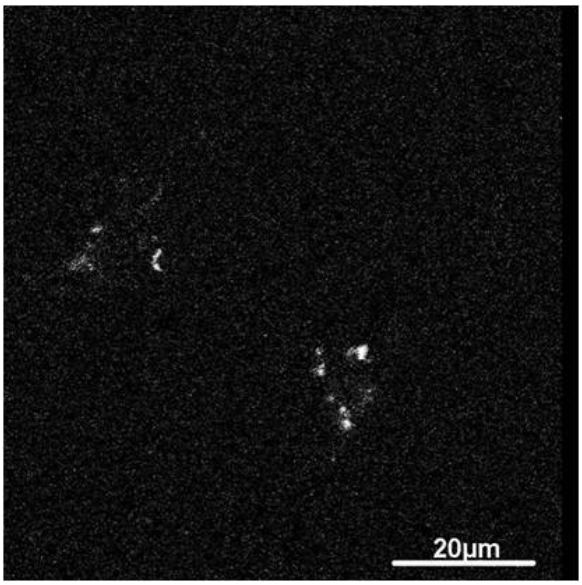

Figure C.2: Weak CD24 signal makes it hard to distinguish the entire cell area

imaged and cells with +3 standard deviations from the unstained mean were treated as positive and all other cells were treated as negative for a particular antibody.